Chinese Chemical Letters 33 (2022) 2327–2344

Contents lists available at ScienceDirect

Chinese Chemical Letters

journal homepage: www.elsevier.com/locate/cclet

Metallic glasses and metallic glass nanostructures for functional electrocatalytic applications

Aneeshkumar K.S.[a,b], Jinsen Tian[a,c,*], Jun Shen[a]

[a] College of Mechatronics and Control Engineering, Shenzhen University, Shenzhen 518060, China
[b] Key Laboratory of Optoelectronic Devices and Systems of Ministry of Education and Guangdong Province, College of Physics and Optoelectronic Engineering, Shenzhen University, Shenzhen 518060, China
[c] Shenzhen Key Laboratory of High Performance Nontraditional Manufacturing, College of Mechatronics and Control Engineering, Shenzhen University, Shenzhen 518060, China

ARTICLE INFO

Article history:
Received 16 October 2021
Revised 9 November 2021
Accepted 7 December 2021
Available online 12 December 2021

Keywords:
Metallic glasses
Nanostructures
Electrocatalytic applications
Reaction mechanism
Fabrication

ABSTRACT

This brief review reports the recent advancement of metallic glasses and metallic glass nanostructures for functional electrocatalytic applications. Metallic glasses (MGs) or amorphous metals result from quenching the melts at a high cooling rate (*e.g.*, 10^6 K/s), bypassing crystallization. Metallic glasses are devoid of long-range translational order, no defects like grain boundaries, and multiple elements included. Due to these unique structural features, MG′s show distinct and valuable mechanical, physical and chemical properties and therefore were widely studied as a structural material for decades. Even though MGs were proposed for catalytic applications earlier, a comprehensive study or attempt to apply these materials successfully in electrocatalytic applications are few since the intrinsic surface area is comparably lesser. A rejuvenated interest among the research community for applying various novel strategies in catalytic applications of MGs is highlighted in the present review. Theoretical approaches using density functional theory (DFT) and high-throughput screening assisted with machine learning paradigm advances the discovery of new MGs, which demonstrated high potential for catalytic applications. We focus on the basic features and recent advances in the MGs for catalytic applications like electrocatalytic water splitting reactions like HER, OER, fuel cell reactions like ORR, alcohol oxidation reactions like MOR, EOR, and degradation of harmful organic dyes from the industrial effluents. The presently advancing strategies for enhancing the performance of these metallic glass electrocatalysts through nanostructuring and high-throughput screening are discussed. The unique atomic-scale structural mechanism of the metallic glasses, which can favor the development of high-performance electrocatalysts even comparable to currently available precious-metal-based catalysts, will be discussed. Finally, we also give future directions on designing novel and superior metallic glass-based advanced catalysts.

1. Introduction

Even though glasses formed by quenching the molten liquid have been familiar for the world for centuries with extensive applications, the melt quenching of metals to form glassy metals was successful about 60 years back only. Metallic glasses (MGs) or amorphous metal alloys are innovative materials formed by rapidly cooling a melt to avoid crystallization and were first observed in Au–Si binary metallic alloys in 1960 by Duwez and co-authors [1]. The amorphous phase refers to the non-equilibrium metastable phase that arises during the manufacturing of MG by supplying energy to bring them from an equilibrium crystalline state to a high non-equilibrium state and then quenched to the desired metastable phase. MGs with highly disordered defect-free atomic structures, unique physical and chemical properties have attracted a wide range of research for different applications [2,3]. Due to the excellent mechanical properties of MGs like high yield strength, high hardness, high elastic strain limits, high wear, and corrosion resistance, electrical conductivity, MG materials were extensively reported for structural materials [4]. In addition, some of the functional applications of MGs were reported in biodegradable implants, energy harvesting devices, and electrochemical devices [5]. Several researchers attempted electrocatalytic applications of metallic glassy materials since these materials exhibited essential features required for an electrocatalyst like high conductivity, strong corrosion-resistance, environmentally friendly nature

* Corresponding author.
E-mail address: jstian@szu.edu.cn (J. Tian).

https://doi.org/10.1016/j.cclet.2021.12.013
1001-8417/

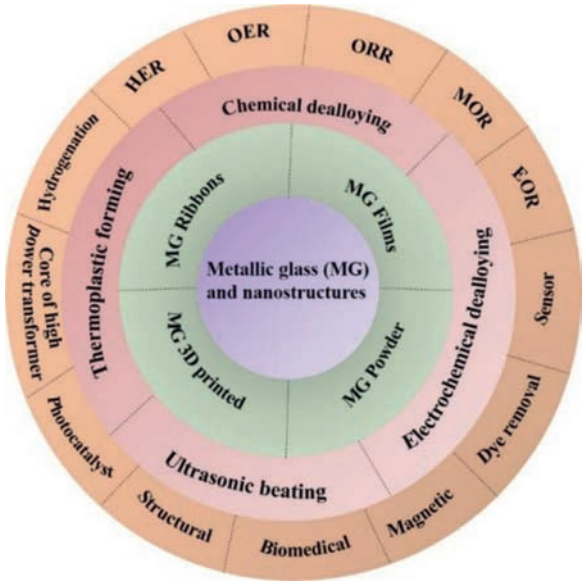

Scheme 1. Schematic illustration of the MGs and MGNs for various catalytic and other significant applications.

and therefore is considered as hot research in industrial electrocatalyst applications for energy conversion and storage. Nanostructures grown on the surface of metallic glass or otherwise called metallic glass nanostructures (MGNs), which combine both the features of nanomaterials and the amorphous phase recently instigate to found remarkable success for catalytic applications and researchers are in search of novel catalysts based on MGs with excellent catalytic activity. Nanomaterials are well established for their unique surface structure and the surface quantum confinement effects that offered novel structural, mechanical, chemical, and optical properties. Thus, nanomaterials were extensively reported for electrochemical applications. Recently, the rapidly advancing MGs and MGNs are receiving rejuvenated attention for various catalytic applications due to their notable performance such as high activity, long-term stability, improved surface area for MGNs, and, more favourably, industrial feasibility. Bulk metallic glasses (BMGs) constituting more than three component elements can reduce the high cooling rate requirement of MGs to hundreds of Kelvin per second and have a thickness of a few inches (typically referred to as critical casting thickness exceeding 1 mm through copper mold casting) also shows improved glass-forming abilities. BMGs constituting several elements and abundant uncoordinated sites are believed to have strong potential in many catalytic applications since the presence of different elements may deliver a wide range of catalytic activity. Even though there are few review articles published describing the electrocatalytic applications of MGs, the correlation between the most recent developments in manufacturing novel MGs, MGNs, and their electrocatalytic applications need to be addressed [6,7]. In this mini-review, the goal is to: 1) outline the fundamental and recent manufacturing techniques of MGs and MGNs toward the realization of novel electrocatalysts, 2) discuss the latest advances in applying novel strategies to be applied for realizing new metallic glass-based catalysts and, 3) report the recent developments in catalyst application of MGs by discussing the MGs and MGNs based on specific feature utilized for catalyst application and their relation with the unique structure of MGs and MGNs. A brief schematic of various applications is shown in Scheme 1. For the reader′s convenience and broad understanding, the fundamental chemistry of the catalytic reactions with some of the well-known fabrication techniques for developing MGs is detailed. To conclude, a report on future vision, challenges, and further opportunities that need to be foreseen towards the further advancement in this research field is given. All the potentials in this review are reported with reference RHE (reversible hydrogen electrode).

2. Fabrication of MGs and MGNs and structural features

The available physical metallurgy techniques for manufacturing MGs are rapid melt quenching methods like melt spinning, drop/suction casting, high pressure die casting, metal foaming, *etc.* Melt spinning is the most popular of these techniques in preparing thin MG ribbons, which can be used as a free-standing electrode in electrolytes. All the quenching techniques mentioned use a master alloy composed of arc melting high purity elements. Fig. 1A schematically shows the time-temperature transformation (TTT) curve for MGs or, in general, for any metallic materials. At a low cooling rate, the melt crystallizes into solid by thermodynamic transformation while high cooling rates vitrify to disordered amorphous phase through the supercooled region. Hence the highly disordered non-equilibrium solid or metallic glass is formed. As the melt cools slowly, crystallization occurs, as shown in TTT diagram. The highly dense and the random atomic packing in MG′s are the most projecting features compared to ordered crystalline materials. Even though it is difficult to visualize the local structure present in the amorphous metals directly, pair distribution function curves (PDF) obtained from the Fourier transform of scattering data can indirectly determine the interatomic distance distribution between pairs of atoms. The PDF curves indirectly determine the local structure present in any materials, which are not unattainable with the conventional X-ray diffraction experiments. Y.Q. Cheng *et al.* reported the pair distribution function calculated using a combination of ab initio molecular dynamics (MD) and embedded atom method (EAM) MD simulations for $Cu_{46}Zr_{47}Al_7$ MG is shown in Fig. 1B [8]. It is understood that the broad PDF derived for MG in Fig. 1B signifies the amorphous state, while sharp peaks in PDF will be observed in the crystalline form. The bond shortening for Cu-Al shown in Fig. 1B marks the disordered microstructure present in MG. It is relatively elusive to experimentally characterize the complex disordered atomic structure of MG′s using conventional diffraction and spectroscopic techniques. Therefore, state-of-the-art angstrom-beam electron diffraction (ABED), atomic electron tomography (AET) reconstruction method and modern theoretical simulations characterized the short to medium range order in MGs [9–11]. An experimental schematic for ABED is shown in Fig. 2A. The diffraction pattern from ABED using a narrow electron beam (FWHM $\sim$ 3Å) gives diffraction spots corresponding to local clusters like microstructures, and the experimental clusters are simulated using Voronoi polyhedral [12]. The experimental and simulated short-range ordered (SRO) clusters are given in Fig. 2B. The local structure shown in Fig. 2B consists of experimental and simulated locally distorted icosahedron with 2-, 3-, and 5-fold symmetry with the simulated pattern based on Voronoi polyhedra designed by building bisecting planes along with the line linking the central atom and its neighbours.

Recently researchers investigated and experimentally verified anisotropic three-dimensional shapes of medium-range order (MRO) investigated using AET are given in Fig. 2C [10]. The discovery of short and medium rage local order in MG′s plays a decisive role in determining the macroscopic properties, suggesting the heterogeneous structural features at the nanoscale. Even though the three-dimensional atomic packing of SRO is geometrically frustrated or disordered, some SRO structures connect to form crystal-like superclusters and give rise to MRO clusters. The MRO clusters show the face-centered cubic (fcc), hexagonal close-packed (hcp), body-centered cubic (bcc), and simple cubic (sc) coexisting in the MGs. The local structure present in the nanoscale is believed to be crucial for catalytic properties, and its

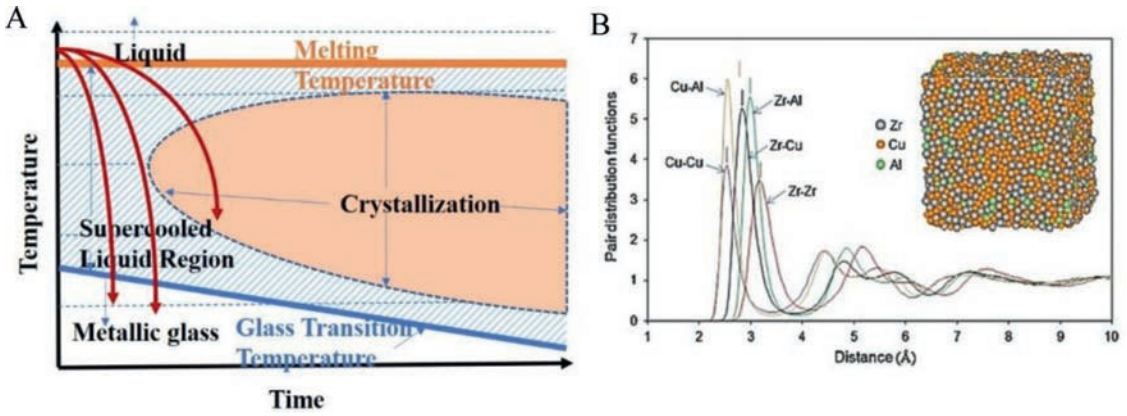

Fig. 1. (A) Schematic of the characteristic time-temperature-transformation (TTT) curve of MGs. (B) Typical radial distribution for $Cu_{46}Zr_{47}Al_7$ MG using advanced simulation algorithms. Reproduced with permission [8]. Copyright 2009, APS Physics.

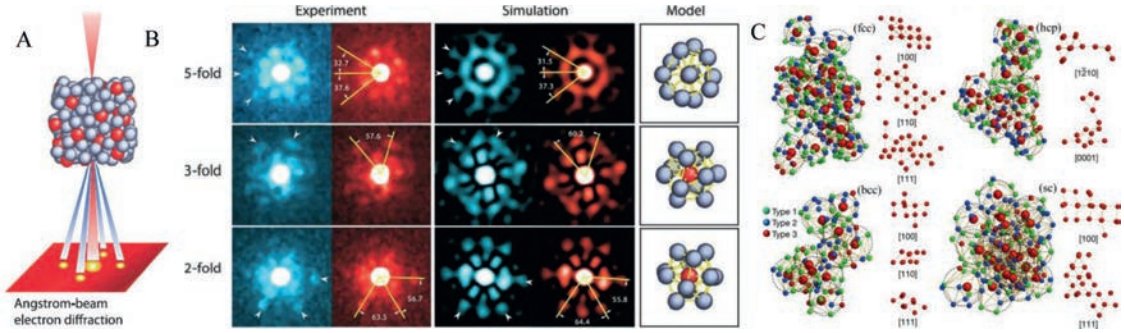

Fig. 2. (A) Experimental procedure of ABED of an icosahedral cluster [12]. (B) Comparison between experimental and simulated ABED patterns of icosahedral clusters in a $Zr_{80}Pt_{20}$ metallic glass. Arrowheads indicate characteristic diffraction spots of the icosahedral order. Reproduced with permission [12]. Copyright 2013, American Association for the Advancement of Science. (C) Fcc, hcp, bcc, and sc-like MROs, consisting of 22, 14, 11, and 23 solute centres (large red spheres), respectively. The solvent atoms have been removed to better visualize the crystal-like MROs, and the solute centres are orientated along the fcc, hcp, bcc, and sc zone axes. Reproduced with permission [10]. Copyright 2021, Nature publishing group.

understanding is vital for developing new applications for MGs. Yoshihiko *et al.* investigated the local atomic ordering in Pd–Ni–P BMG′s and verified that the nanoscale phase separation is not due to the compositional fluctuation rather than a structural modulation initially present at the glass transition [13]. Metallic glasses have physical properties far superior to their crystalline counterparts, useful for developing stable industrial electrocatalysts. The fracture strength of the metallic glasses is in the Giga pascal (GPa) range and achieves a high Young′s modulus of 4–6 GPa for cobalt-based metallic glasses [14,15]. Further, MG′s have total range toughness value, low mechanical damping, and good corrosion resistance. For developing durable catalysts, focus on MGs showing excellent mechanical properties and anti-corrosion features for functional applications like catalysis for long-time operations is to be developed. In addition, MG′s can be nanopatterned to the same length scales as conventional catalysts and are an added benefit while applying as electrodes. There are various techniques for nanostructuring the MG′s. The principal methods for forming metallic glass nanostructures (MGN′s) are nanolithography, dealloying chemically or electrochemically, thermoplastic forming, physical synthesis methods like melt spinning, gas atomization, combinatorial sputtering techniques, *etc.* This section will discuss some of the techniques used for synthesizing MGs, such as melt spinning, thermoplastic forming, physical and chemical vapor deposition (PVD, CVD), additive manufacturing.

2.1. Melt spinning

The most common and popular technique for producing MG ribbons is the chilled melt spinning method. In this technique, the desired microstructure for the melt-spun MG ribbon depends on various factors, including the alloy composition, the cooling rate, melt position, and wedge angle. A homogenous master alloy with a pre-designed elemental composition is prepared through the arc melting technique. The master alloy thus manufactured is further melted in a quartz crucible, and the melted liquid is ejected onto a copper single-roller spinning wheel. The optimized rotating speed is fixed initially, and the MG ribbons of approximate thickness 20–80 μm thickness are manufactured. The rate of cooling needs to be optimized from the time-temperature transformation (TTT) diagram. Since metallic glass ribbons are applied in various industrial applications such as cores of transformers and are an effective alternative to conventional crystalline materials with superior mechanical properties, the as-spun ribbons are manufactured in bulk quantity. Thus, the melt spinning technique offers a constant market for real-world catalytic applications. In electrocatalyst applications, the melt-spun ribbons may be cut to required sizes and have the advantage of free-standing in electrolytes with high durability and reusability [16]. Figs. 3A-C shows the schematic of manufacturing MG ribbons through melt spinning. The advantages of using the MG ribbons in electrocatalytic application is that ribbons can be directly used as electrode without any polymer binders without losing the intrinsic conductivity. Melt spinning is industrially implemented. The disadvantage is that strength of ribbons in electrolyte medium where consistent research of corrosion improvement of MG ribbons is required.

2.2. Thermoplastic forming

Thermoplastic forming (TPF) is a miniature fabrication technique for manufacturing micro to nanostructures for BMG with

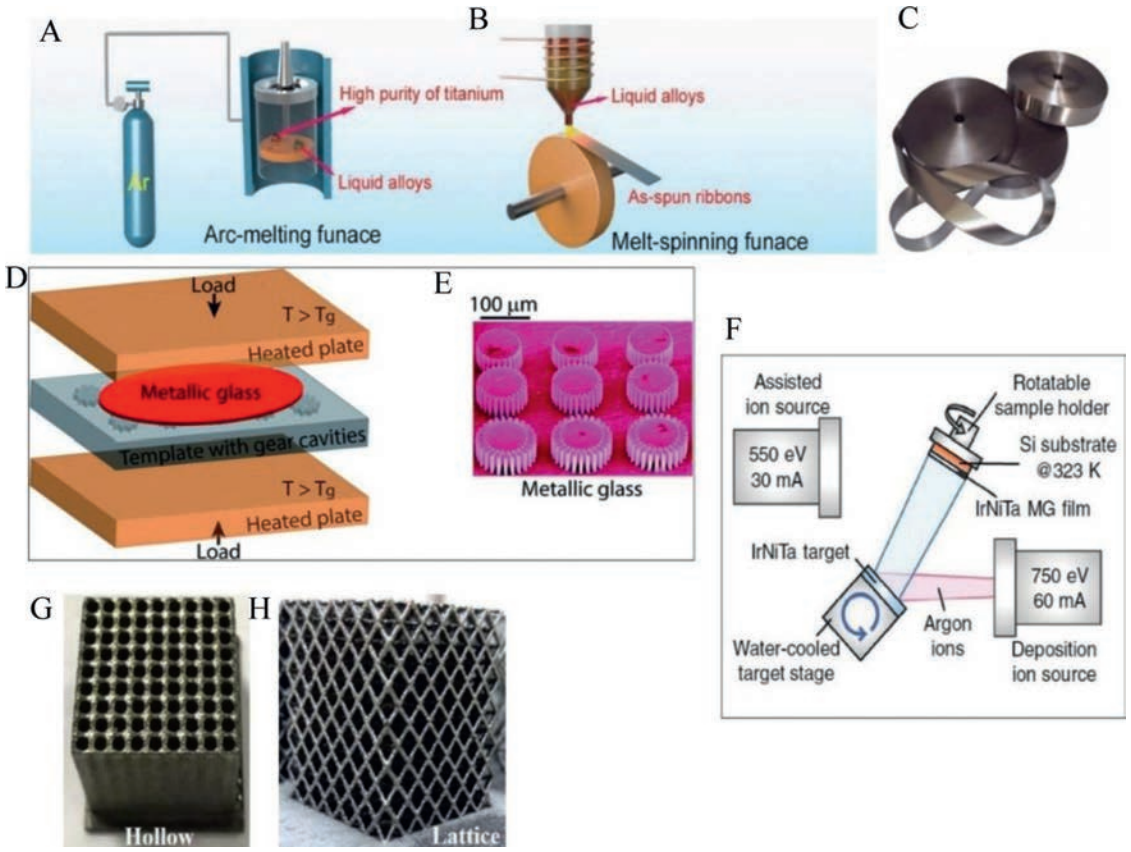

Fig. 3. (A) Arc melting furnace. (B) Melt-spinning furnace. (C) As-prepared melt-spun MG ribbons. (D, E) Schematic illustration of parallel plate thermoplastic forming (TPF) of MGs. Load is applied to the template and MG assembly, heated above Tg and the viscous MG fills the template cavities with MG micro gear specimens, Reproduced with permission [18]. Copyright 2013, The Royal Society of Chemistry. (F) Schematic diagram illustrating deposition of the $Ir_{25}Ni_{33}Ta_{42}$ MG film on Si substrates, Reproduced with permission [20]. Copyright 2019, WILEY-VCH Verlag GmbH & Co. KGaA, Weinheim. (G, H) 3D-printed BMGs with hollow and lattice structure. Reproduced with permission [22]. Copyright 2018, Elsevier Ltd.

different shapes. The TPF technique uses the severe softening of the BMG on heating above the glass transition temperature (supercooled liquid region, SLCR) and manufactures specimens of desired shapes [17,18]. During the thermoplastic forming process, the preferred parameters are the low viscosity of the supercooled liquid and higher processing time. The melt in the supercooled region is pressed into moulds on templates of desired shapes, and after BMG miniature forming, the template is dissolved to release the BMG specimen apart. The nanostructures thus prepared on MG surfaces have found significant electrocatalytic applications. Figs. 3D and E show the MG-based micro gears manufactured using TPF. The advantage of this technique is even though nanostructures of complex shapes can be manufactured, and there are demerits for TPF technique like all the elements cannot be included, selection of proper parameters for thermoplastic forming. Inclusion of other catalytic active elements using galvanic displacement, electrochemical displacement is in progress.

2.3. Physical and chemical vapor deposition (PVD, CVD)

In the physical vapor deposition technique, the desired material in solid form is vaporized, and the vapours are deposited onto a target. One popular method is sputter deposition. In sputtering, the target material is bombarded with glow plasma or a sputtering gas that takes away the material as vapor and then deposits on the substrate [19,20]. Pulsed laser deposition (PLD) is another technique in which a high-powered laser vaporizes the material. Fig. 3F shows the synthesis of IrNiTa MG thin film using ion vapor deposition. The application of thin-film metallic glasses for electrocatalysis is still in progress.

2.4. Additive manufacturing

Additive manufacturing or 3D printing is a widely reported metallurgical technique to manufacture metallic alloys and polymers with distinct geometries and porous micro/nanostructures. Powder-based layer-by-layer shaping and consolidation process finely tailors microstructure, porosity, shape, and size of the deposited materials. Pauly used 3D printing using selective laser melting (SLM) for fabricating Fe-based MG′s [21]. The advantage of this manufacturing technique is to develop MG′s even with the poor glass-forming ability to overcome the size limitation. The graded structures induced in these MG′s have a tremendous effect on the physical and chemical properties, potentially beneficial in developing MG-based catalysts [22]. Figs. 3G and H show the typical BMG structures like hollow and lattice-type using 3D printing. The main advantage of SLM is that a wide range of materials can be used and the disadvantages are that the manufacturing accuracy is limited by the size of particles, and the mechanical strength of as-fabricated parts is normally lower than that of the counterpart bulk material

3. Electrocatalytic performance

Developing catalysts for producing hydrogen fuel as a substitute for the currently depleting fossil fuel is in great demand in the energy storage/conversion sector. Several researchers are developing

alternate green energy sources considering the foreseen shortage of non-renewable and harmful CO_2 releasing fossil fuels. MGs and MGNs find application as electrode material in various electrocatalytic reactions like electrochemical water splitting reactions like HER and OER, ORR, alcohol oxidation like MOR, EOR, Fuel cells, *etc.*

3.1. Hydrogen evolution reaction (HER)

Hydrogen (H_2) fuel is considered the most attractive substitute for the current non-renewable fossil fuels since H_2 has substantial mass-energy density and an environmentally friendly nature. It is a renewable fuel too. The generation of hydrogen (H_2) through the electrochemical water splitting technique is highly efficient since water is freely abundant in the earth, and this technique is free of carbon. Hydrogen evolution reaction, HER, is a half-cell reaction ($2H^+ + 2e^- \rightarrow H_2$) on the cathode of the electrochemical water splitting technique. For efficient and accelerated production of H_2 fuel through HER response, catalytically active and highly durable electrocatalyst is required. Presently, most of the electrocatalysts for HER are crystalline materials, including metal oxides [23–25], nitrides [26], phosphides [27], carbides [28], sulfides [25,29–31], and their products in carbon matrices like carbon nanotubes [32,33], graphene [34], *etc.* One of the main demerits of the crystalline catalysts is the instability in structure while performing the long-term operation in an electrolyte medium. The scaling up of these laboratory-made materials to huge industrial applications needs to be realized. Researchers and industrialists put a lot of effort into finding an alternative for crystalline catalysts. The metallic glass and its surface-modified MGN′s are significant for catalyst applications and a highly promising substitute for crystalline catalysts due to the structural heterogeneity at the nanoscale and the defect-free microstructure. The standard electrocatalyst for HER reactions is based on noble metals like Pt, Pd, *etc.* Metallic glasses based on these noble metals were found to be catalytically active compared to standard Pt catalysts. Since the noble metals are precious and their supply is limited worldwide, transition metal (Fe, Co, Ni, Ti, and Cu) based metallic glasses were also attempted to achieve the activity of noble metal-based catalysts [35]. It may be seen that surface-modified noble metal-based and transition metal MG′s show appreciable catalytic performance towards HER reaction and additional features much comparable or even improved than the crystalline catalysts. Some of the recently reported MG based catalysts are $Pd_{40}Ni_{10}Cu_{30}P_{20}$ [36], $Pt_{20}Pd_{20}Cu_{20}Ni_{20}P_{20}$ [37], $Pt_{57.5}Cu_{14.7}Ni_{5.3}P_{22.5}$ [38], Ni-Zr-Ti [39], Pd-Ni-P [40], PdCuNi-S [41], NiZrTiPt [42], np-PdFePC [43], Cu-Mo [44], IrNiTa [20], $Ni_{61}Zr_{36}Mo_3$ [45], $Cu_{60}Ti_{37}Mo_3$ [46], $Fe_{40}Ni_{20}Co_{20}P_{15}C_5$ [47]. The catalytic features of the recently reported metallic glasses are summarized in Table 1. Noble metal-based metallic glasses like $Pd_{40}Ni_{10}Cu_{30}P_{20}$, $Pt_{57.5}Cu_{14.7}Ni_{5.3}P_{22.5}$ showed excellent self-stabilizing behavior during long-term HER operation and improved catalytic activity on continuous cycling. The standard Pt/C crystalline catalyst exhibited an overpotential of 32 mV with a Tafel slope of 30 mV/dec [48].

Pd-Cu-Ni-P MG ribbon, a well-known glass former, was attempted for HER electrocatalyst with the free-standing ability of MG ribbons in electrolytes and reported excellent electrocatalytic features [36]. The HER activity, durability, and comparison with other reported catalysts are shown in Figs. 4A-D. The catalytic activity increases to a maximum upon cycling and decreases very slowly while crystalline Pt/C standard catalyst shows a decay in catalytic activity on continuous cycling. The relative current density increases to 120% upon cycling and then stabilizes to total efficiency upon further cycling. Standard Pt/C catalyst shows a degradation to 40% upon cycling. Pd-Ni-Cu-P MG ribbon showed an overpotential of 76 mV at a current density of 10 mA/cm^2 with a Tafel slope of 58 mV/dec. On the other hand, standard Pt/C electrocatalyst needs an overpotential of 108 mV at a current density of 10 mA/cm^2. Taking account of the improved glass-forming ability and the wide supercooled region, Yuqiang *et al.* thermoplastically formed nanowires of Pt@Pd-NiCu-P and is shown in Figs. 4E-G [49]. The nanowires of Pd-Ni-Cu-P BMG displayed in Fig. 4F were electrochemically deposited with Pt as demonstrated in Fig. 4G, and the Pt@Pd-Ni-Cu-P MG showed an excellent catalytic activity towards HER in acid medium with an overpotential of 48.5 mV as demonstrated in Fig. 4H and a low Tafel slope of 19.8 mV/dec (Fig. 4I) which is less than the overpotential for standard Pt/C electrocatalyst (36 mV) as measured. The Pt@Pd-Ni-Cu-P MG maintained constant catalytic activity even for 500 Hr, as shown by the discontinuous current density in Fig. 4J. The higher electrocatalytic activity of the MGs arises due to the metastable heterogenous surface character, favourable electron transfer, and selective dealloying in the electrolyte solution. The active catalytic and atomic mechanisms of these MG electrocatalysts will be discussed in section 6. Thus, metallic glass electrocatalyst Pt@Pd-Ni-Cu-P formed by thermoplastic forming offers a superior catalytic activity for HER than the existing standard Pt, or crystalline catalysts developed so far. F. Chu *et al.* reported $Pd_{40}Cu_{30}Ni_{10}P_{20}$ MG, when plastically deformed through high-pressure torsion (HPT), exhibited excellent HER catalytic activity as schematically displayed schematically in Fig. 5A [50]. The overpotential of the deformed plastic MG is 76 mV and 209 mV in 0.5 mol/L H_2SO_4 and 1.0 mol/L KOH, respectively as shown in the linear polarization curves in Figs. 5B and C. The strategy of plastic deformation through HPT in the Pd-based MG introduces more flow units on the amorphous matrix and significantly improves the electrocatalytic HER performance in acid and alkaline medium. Wang *et al.* synthesized a 15 nm thick $Ir_{25}Ni_{33}Ta_{42}$ MG film on Si substrate with an ultra-low Ir loading of 8.14 μg/cm^2 and exhibited superior HER activity [20]. The central catalytic feature of IrNiTa film includes a turnover frequency (TOF) value of 1.76 and 19.3 H_2/s at 50 and 100 mV, respectively, claiming to be outperforming any of the reported MG based electrocatalysts. The overpotential for IrNiTa film at 10 mA/cm^2 in 0.5 mol/L H_2SO_4 is 99 mV with a small Tafel slope value of 35 mV/dec. Comparison of IrNiTa MG film with other reported catalysts in terms of Tafel slope and TOF is shown in Fig. 6.

Several research groups attempted to replace the expensive noble metal-based MG electrocatalysts with transition metal-based MG electrocatalysts. Fe-based MGs are popular in the transition metal-based MGs for electrocatalyst applications since iron has widened valance band, thus lower activation energy and better electron transferability. Zhang *et al.* synthesized Fe-based ($Fe_{40}Co_{40}P_{13}C_7$) MG ribbons through the industrial melt spinning technique [51]. The reported overpotential for the Fe-based MG is 118 mV in an acidic medium, and the overpotential remained constant for 20 Hr without degradation. Yongwen Tan *et al.* synthesized $Ni_{40}Fe_{40}P_{20}$ MG ribbons and showed superior catalytic activities and minimum corrosion [52]. The authors reported an exchange current density (a measure of the rate of H_2 production) as 0.024 mA/cm^2, comparable to standard Pt catalyst. Kaiyao Wu *et al.* synthesized $Fe_{78}Si_9B_{13}$ nano MG glass through melt-spinning followed by HPT treatment (Fig. 7) [53]. HPT induced slight unique crystallization; meanwhile, abundant flow regions/interfaces were formed, which promoted the HER catalytic activity of the nano glass. HPT deformed $Fe_{78}Si_9B_{13}$ nano MG glass requires a small overpotential of 112 mV for alkaline HER reaction. Transition metal-based MGs were attempted enormously as an electrocatalyst and attempts for enhancing the catalytic activity by nanostructuring and several novel fabrication techniques discussed in Section 4.

3.2. Oxygen evolution reaction

Oxygen evolution reaction (OER) is a crucial step in electrochemical water splitting, fuel cells, lithium-ion batteries, occur-

Table 1
Summary of metallic glass catalysts with their catalyst performances.

Sr. No.	Metallic glass catalyst	Catalyst performance	Ref.
1	$Ir_{25}Ni_{33}Ta_{42}$ MG film	HER electrocatalyst with $\eta_{10} = 100$ mV, Tafel slope = 35 mV/dec	[20]
2	$Pd_{40}Ni_{10}Cu_{30}P_{20}$ MG ribbon	HER electrocatalyst with $\eta_{10} = 76$ mV, Tafel slope = 24 mV/dec (Acid electrolyte)	[36]
3	$Pt_{20}Pd_{20}Cu_{20}Ni_{20}P_{20}$ high entropy MG ribbon	HER electrocatalyst with $\eta_{10} = 32$ mV (Acid electrolyte) and $\eta_{10} = 62$ mV (Alkaline electrolyte)	[37]
4	$Pt_{57.5}Cu_{14.7}Ni_{15.3}P_{22.5}$ BMG nanowire through TPF	High electrocatalytic activity toward CO, methanol, and ethanol oxidation	[38]
5	$Ni_{40}Zr_{40}Ti_{20}$ wire	HER electrocatalyst with $\eta_{10} = 78$ mV, Tafel slope = 42.4 mV/dec (Alkaline electrolyte)	[39]
6	Pd-Ni-P nanoparticles	High electrocatalytic activity toward methanol oxidation reaction (MOR)	[40]
7	Pd-Cu-Ni-S MG ribbon	Dealloyed MG ribbon as efficient HER electrocatalyst $\eta_{10} = 48$ mV, Tafel slope = 35 mV/dec (Acid electrolyte)	[41]
8	$Ni_{40}Zr_{40}Ti_{17}Pt_3$ MG ribbon	Dealloyed MG ribbon with honeycombed structure as efficient HER electrocatalyst $\eta_{10} = 37$ mV, Tafel slope = 30 mV/dec (Alkaline electrolyte)	[42]
9	Nanoporous pdFePC MG ribbon	Dealloyed MG ribbon as efficient HER electrocatalyst $\eta_{10} = 45$ mV, Tafel slope = 30 mV/dec (Acid electrolyte)	[43]
10	CuMo dealloyed from Al-Cu-Mo ribbon	Dealloyed MG ribbon as efficient HER electrocatalyst $\eta_{10} = 97$ mV, Tafel slope = 100 mV/dec (Alkaline electrolyte)	[44]
11	$Ni_{61}Zr_{36}Mo_3$ MG ribbon	Dealloyed MG ribbon as efficient HER electrocatalyst $\eta_{20} = 71$ mV, Tafel slope = 57 mV/dec (Alkaline electrolyte)	[45]
12	$Cu_{60}Ti_{37}Mo_3$ MG ribbon	Dealloyed MG ribbon as efficient HER electrocatalyst $\eta_{100} = 220$ mV (Alkaline electrolyte)	[46]
13	$Fe_{40}Ni_{20}Co_{20}P_{15}C_5$ MG ribbon	Dealloyed MG ribbon $\eta_{10} = 128$ mV (HER-Acidic electrolyte), $\eta_{10} = 236$ mV (HER-Alkaline electrolyte), $\eta_{10} = 278$ mV (OER-Alkaline electrolyte)	[47]
14	Pt@Pd-Ni-Cu-P TPF formed wire	HER electrocatalyst $\eta_{10} = 48.5$ mV, Tafel slope = 19.8 mV/dec (Acidic electrolyte)	[49]
15	$Pd_{40}Cu_{30}Ni_{10}P_{20}$ (HPT)	HER electrocatalyst $\eta_{10} = 76$ mV, (Acidic electrolyte) $\eta_{10} = 209$ mV (Alkaline electrolyte)	[50]
16	$Fe_{40}Co_{40}P_{13}C_7$	HER electrocatalyst $\eta_{10} = 118$ mV, Tafel slope = 46 mV/dec (Acidic electrolyte)	[51]
17	$Ni_{40}Fe_{40}P_{20}$	HER, OER electrocatalyst $\eta_{10} = 193$ mV, Tafel slope = 65 mV/dec (HER-Acidic electrolyte) $H_{10} = 270$ mV, Tafel slope = 89 mV/dec (HER-Alkaline electrolyte) $\eta_{10} = 270$ mV, Tafel slope = 35 mV/dec (OER-Alkaline electrolyte)	[52]
18	$Fe_{78}Si_9B_{13}$ (HPT)	HER electrocatalyst $\eta_{10} = 112$ mV (Alkaline electrolyte)	[53]
19	FeCoNiP MG ribbon	OER electrocatalyst $\eta_{10} = 497$ mV (Acidic electrolyte) $\eta_{10} = 281$ mV (Alkaline electrolyte)	[55]
20	$Ni_{40}Fe_{40}P_{20}$	OER electrocatalyst $\eta_{10} = 540$ mV (Acidic electrolyte) $\eta_{10} = 219$ mV (Alkaline electrolyte)	[56]
21	$Zr_{35}Ti_{30}Cu_{8.25}Be_{26.75}$	Fuel cell-flow field with power density of 294 mW/cm^2	[59]
22	$Pt_{57.5}Cu_{14.7}Ni_{53}P_{22.5}$	Methanol oxidation (Activation energy = 22 kJ/mol, Pd = 38 kJ/mol), Ethanol oxidation (Activation energy = 17 kJ/mol, Pd = 30 kJ/mol)	[61]
23	Pd-Au-Si on Si/SiO_2	Electrocatalyst for methanol oxidation reaction (MOR) in alkaline medium, high CO poisoning tolerance with catalyst stability for long time	[62]
24	$Fe_{67.5}B_{22.5}Nd_{6.3}Nb_{3.7}$	Sensor	[63]
25	$Fe_{33}Zr_{67}$	Multi-functional sensor in electronic skin	[64]
26	$Zr_{55}Al_{10}Ni_5Cu_{30}$	Pressure sensor	[65]
27	$Pd_{78}Cu_5Si_{17}$	MEMS hydrogen sensor	[66]
28	$Fe_{78}Si_9B_{13}$	Electoccatalyst for electrochemical dye degradation	[68]
29	$Fe_{78}Si_9B_{13}$ MG powder	MG powders using ultrasonic vibration for improved dye degradation	[69]
30	$Fe_{68}Mo_5Ni_5Cr_2P_{12.5}C_5B_{2.5}$/Cu MG composite	3D printed MG catalyst for dye degradation	[70]
31	$Fe_{73.5}Si_{13.5}B_9Cu_1Nb_3$	A rejuvenated degradation from annealing the MG with evolution of crystalline phases.	[71]
32	$Fe_{76}B_{12}Si_9Y_{13}$	High degradation efficiency towards methyl orange in strong acidic and near neutral environments compared to crystalline zero-valent iron (ZVI) powders and other Fe-based metallic glasses	[72]
33	$Pt_{57.5}Cu_{14.7}Ni_{5.3}P_{22.5}$, $Pd_{43}Ni_{10}Cu_{27}P_{20}$	Electrocatalyst towards high activity in HOR	[73]
34	Pd-Au-Ag-Ti	ORR electrocatalyst synthesized through combinatorial screening	[77]
35	Fe-Si-B-Nb	Azo dye degradation catalyst 200 times faster than Fe powders	[79]
36	$Ti_{42.5}Zr_{10}Cu_{40}Ni_5Sn_{2.5}$ MG powder	Efficient removal of Cr^{6+} ions	[80]
36	CuO/TiCu	Photocatalyst H_2 evolution	[81]
38	Fe–Co–Ni–Cr–Nb	OER with overpotential 288 mV	[92]
High performing crystalline catalysts			
39	20wt%Pt/C	HER in acidic medium with overpotential of 32 mV and Tafel slope 30 mV/dec	[48]
40	IrO_2	Overpotential of 320 mV for OER in alkaline solution	[54]
41	MoS_2 nanosheets	HER in acidic medium with overpotential of 150 mV and Tafel slope 94 mV/dec	[25]
42	VS_2	The interlayer-expanded VS_2 nanosheets show excellent HER features with overpotential of 43 mV and Tafel slope 36 mV/dec	[31]
43	FeP/Fe_3O_4-CNT	Overpotential of 229 mV for OER in alkaline solution	[33]

ring at the anode. It is given as $4OH^- \rightarrow 2H_2O + O_2 + 4e^-$ in acidic medium and $2H_2O \rightarrow 4H^+ + O_2 + 4e^-$ in alkaline medium. Since OER is a basic reaction for generating electrons and protons for hydrogen evolution reaction in electrochemical water splitting, the overall water splitting rate depends on the OER step. Therefore, it is essential to increase the rate of OER reaction by utilizing highly efficient electrocatalysts. The conventional high-performing OER catalysts are usually made of precious noble metals like Ir, Ru, and Pt and improvement for developing OER catalysts based on transition metals like Ni, Fe, or Co is systematically in progress. The transition metal-based electrocatalysts are found to be highly active for increasing the rate of OER since they have smaller d-orbitals and thus lower crystal-field activation energies, which makes their compounds more active in OER as compared with noble metal oxides (*e.g.*, RuO_2 and IrO_2 [54]). The transition metal-based crystalline OER catalysts are often attached to Ni substrate or glassy ribbons while exposed in an electrolyte medium. The conductivity loss due to contact issues and the instability of the crystalline catalyst materials necessitates fabricating highly disordered transition metal-based MGs as catalysts for OER. S. Jiang *et al.* synthesized FeNiCoP MG alloys using industrial melt spinning technique and reported the OER activity (Figs. 8A-C) [55]. FeNiCoP exhibited a low overpotential of 497 mV and Tafel slope of 79 mV/dec in acidic medium and an overpotential of 281 mV and a Tafel slope of

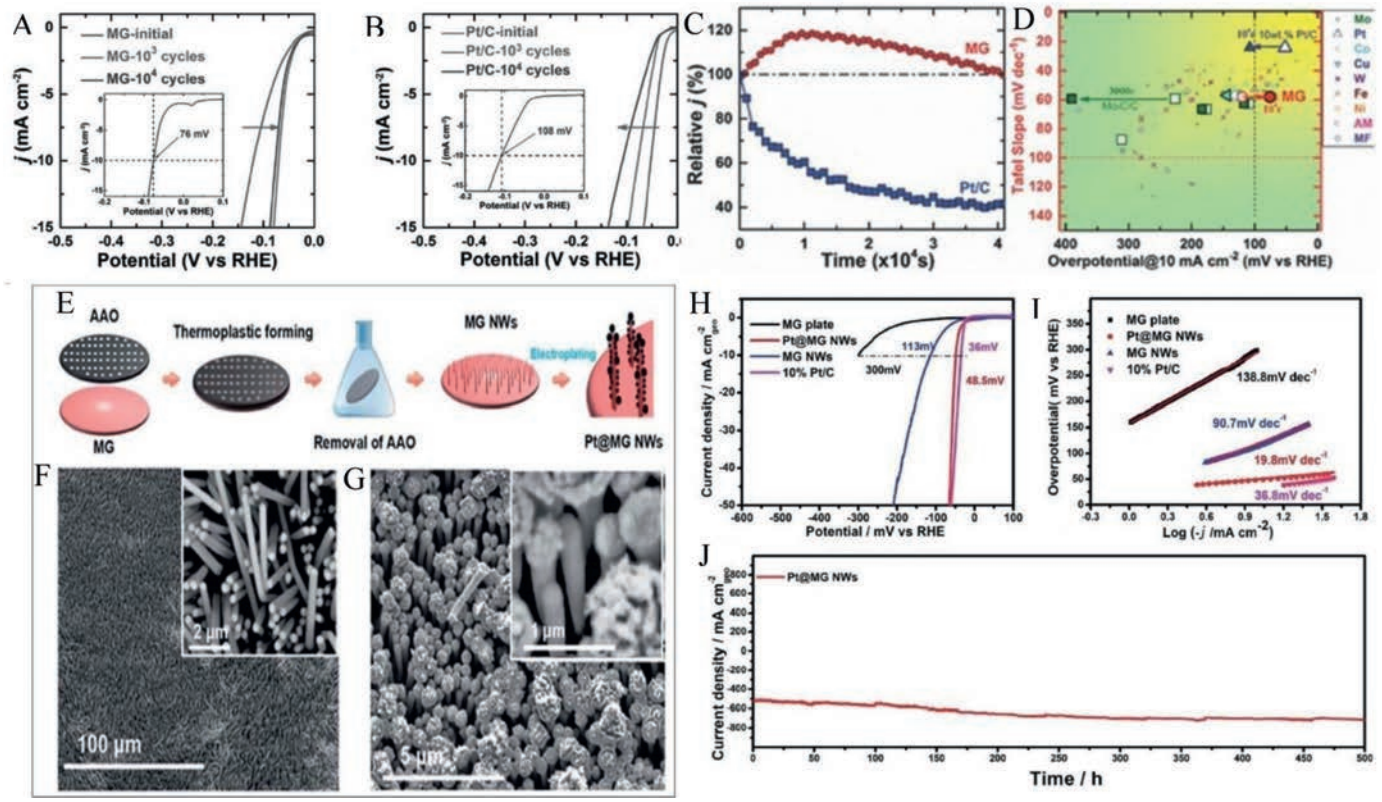

Fig. 4. (A-C) The polarization curves and the durability of Pd-CuNi-P metallic glass catalyst durability compared to the Pt/C catalyst. (D) Comparison of the electrocatalytic performance of the Pd-metallic glass catalyst to variously reported catalysts, Reproduced with permission [36]. Copyright 2016, WILEY-VCH Verlag GmbH & Co. KGaA, Weinheim. (E) Schematics for Pt@MG nanowire fabrication including thermoplastic forming. AAO removal, electroplating of the fine Pt particles. (F, G) SEM images of MG nanowire before electroplating and after electroplating. (H-J) polarization curves, Tafel plot, durability test for 500 Hr. Reproduced with permission [49]. Copyright 2021, The Royal Society of Chemistry.

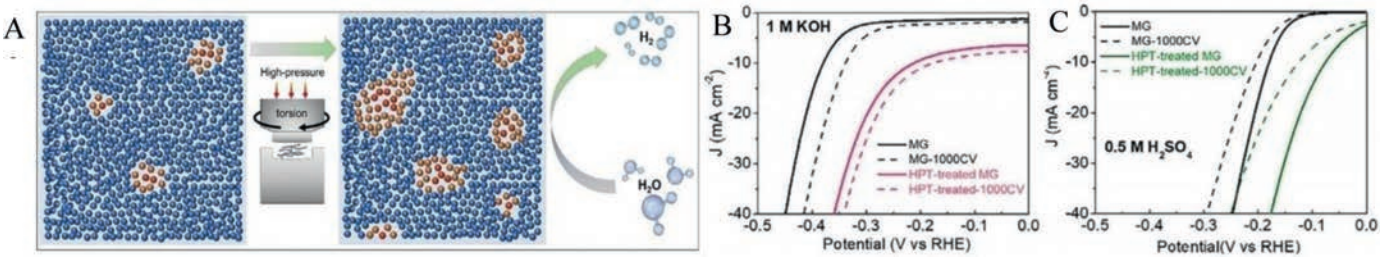

Fig. 5. (A) Schematic diagram of the density of flow units in the amorphous matrix before and after HPT treatment $Pd_{40}Cu_{30}Ni_{10}P_{20}$ and the hydrogen generation process, HER polarization curves in (B) alkaline medium, (C) acidic medium. Reproduced with permission [50]. Copyright 2021, Acta Materialia Inc. Published by Elsevier Ltd.

38 mV/dec in alkaline solutions, respectively as shown in Figs. 8D and E. The FeCoNiP is found to be highly durable in the electrolyte solution (Fig. 8F), and the excellent OER activity arises due to the increase in density of Fe-centered clusters with low coordination number leading to a large number of active sites for high catalytic activity and the synergistic interaction of phosphates and hydroxide intermediate species. Fei Hu *et al.* synthesized $Ni_{40}Fe_{40}P_{20}$ MG ribbons through melt spinning, and an intrinsic overpotential of 280 mV was observed for OER in an alkaline medium [56]. For further enhancing the catalytic activity, dealloying treatment in HNO_3 further reduces the overpotential to 219 mV with a Tafel slope value of 32 mV/dec, and the modified MG ribbon after dealloying treatment is durable even for 25 Hr. Improved electronic conductivity is shown in the EIS spectrum as a semicircle intercepting at low impedance on the x-axis as in Fig. 8G. From EXAFS measurement given in Figs. 8H and I, the authors deduced the presence of metallic bonding Ni–Ni and Fe–Fe and phosphide bonds Ni/Fe with P. The metallic bonds facilitated the electron transport in long distances. In contrast, phosphide bonds facilitated electron transport at medium distances. Moreover, the Ni and Fe atoms are coordinatively unsaturated. All these merits present in the NiFeP MG ribbon catalyst discussed above improved the OER activity.

3.3. MG's in fuel cell applications

Generation of electric power using hydrogen or hydrogen-containing fuels using fuel cells is considered the next generation solution for the current fossil fuel-based internal combustion engines in the automobile industry. Even though the research in the fuel cell is successfully progressing, present fuel cells are operating at low temperatures, and efficiency is considerably affected by increasing the temperature. Currently, available fuel cells are proton exchange membrane fuel cells (PEMFCs) and alkaline fuel cells. PEMFC fuel cells are well-known for transportation and portable

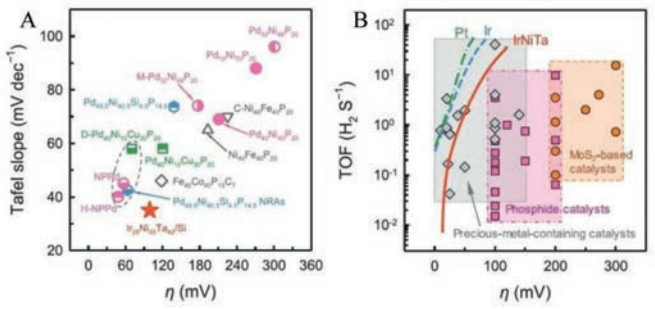

Fig. 6. Comparison of IrNiTa MG film with other reported catalysts. (A) Tafel slope *versus* the overpotential for HER in 0.5 mol/L H_2SO_4. (B) Turnover frequency averaged over all sites in MG film *versus* the overpotential. Reproduced with permission [20]. Copyright 2019, WILEY-VCH Verlag GmbH & Co. KGaA, Weinheim.

applications for their high energy density, high-efficiency energy conversion, and low noise. The major constraint limiting the robustness in PEMFCs is the corrosion of the electrodes while using strongly corrosive acid-electrolyte, and the development of alkaline fuel cells is an alternative. Bipolar plates (BPPs), and critical components of the PEMFC stack in fuel cells need good electrical conductivity, interfacial contact resistance (ICR), corrosion resistance, and high formability [57]. Due to the machining cost and poor mechanical properties, graphite plates in fuel cells were replaced with stainless steel for industrial applications. But the stamping in thin metallic steel plates causes errors, adversely affecting the fuel cell performance. Besides, corrosion-resistant coatings are expensive [58]. Therefore, PEMFC needs low-cost, high-performing material developed through modern fabrication techniques. TPF forming of BMG is one of the superior solutions to be considered as the BMG has good electronic conductivity, highly corrosion resistance properties, and the incorporation of more active elements. Ryan. C. Sekol *et al.* reported a micro fuel cell in which the catalyst layer, gas diffusion layer, and flow fields were fabricated from bulk metallic glass (BMG) using thermoplastic forming (Figs. 9A-E) [59]. The authors used Zr-BMG ($Zr_{35}Ti_{30}Cu_{8.25}Be_{26.75}$) synthesized through TPF as endplates with serpentine flow field current collectors and Pt-BMG ($Pt_{57.5}Cu_{14.7}Ni_{53}P_{22.5}$) TPF formed hierarchical structure (Figs. 9A-E) act as a high surface area catalyst as well as the porous gas diffusion layer. Zr-BMG flow field yielded a high-power density of 294 mW/cm^2, whereas the best power density reported in the literature is 194.3 mW/cm^2. Porous Pt-BMG electrode displays an initial increase in electrochemically active surface area (ECSA) followed by a stable plateau at nearly 8% above the initial ECSA value (Fig. 9F). On the other hand, standard Pt/C shows 60% loss of ECSA after 1000 cycles. These features show the high efficiency and durability of BMG materials for fuel cell applications.

In alkaline fuel cells, the high overpotential requirement for the oxidation–reduction reaction (ORR) results in a loss of catalytic activity. The conventional catalysts based on precious noble metals like Pt/Pd need cost-effective alternatives to develop economic fuel cells. Even though the ORR reaction is an equally significant reduction reaction like the HER reaction, metallic glasses are less reported for ORR catalysts. Chen *et al.* reported AgCu-MG for ORR long-term stability of more than 20 Hr [60]. Authors prepared AgCu-MG through pulse laser deposition, PLD using nickel foam as the substrate. AlCu-MG was transformed to nanocrystalline AgCu (AgCu-NC) by annealing at 300 °C. The initial half-wave potential of MG and nanocrystalline AgCu are identical (0.67 V *vs.* RHE), as shown in Fig. 9G. After 1000 CV cycles, it was noted that the half-wave potential of AgCu-MG increased to 0.78 V *vs.* RHE while that of AgCu-NC decreased to 0.48 V *vs.* RHE as shown in Fig. 9G. thus continuous cycling enhanced the ORR activity of metallic glass form of AgCu while there is a decay in the ORR activity for the nanocrystalline form of AgCu. After 1000 CV continuous cycling, the Cu atoms almost disappeared from the nanocrystalline form of AgCu while Cu gets preserved in AgCu MG even after 1000 CVs as verified from XPS and EDS measurements. Ultraviolet photoelectron spectroscopy (UPS) measurements further supported the reduced etching of Cu. UPS measurement in Figs. 9H and I shows that $E_{\text{cut-off}}$ for AgCu Mg is higher than AgCu-NC, suggesting the higher work function (ϕ) and more energy is consumed to lose electrons, thereby protecting Cu without etching from the MG surface.

Pd-Cu-Ni-P MG nanowires with a high surface area have enhanced methanol oxidation reaction (MOR) activity in alkaline media [61]. The extraordinary methanol activity arises from the free volume present between the atomic clusters in metallic glass, which increases the surface-to-volume ratio and the number of surface interactions. Pd-Ni-Cu-P MG has a lower onset potential (300 mV) for ORR than pure Pd catalyst. The activation energy of Pd-based MG is small for both MOR and EOR, confirming the intrinsic activity toward excellent fuel cell applications. Pd-Au-Si MG nanofilm on Si/SiO^2 is reported as a potential electrode for MOR [62]. The Pd-Au-Si MG, devoid of grain boundaries, enhances the amount of methanol oxidation and provides CO poisoning tolerance and stability at high scan rates (85% higher MOR current density and 50% higher oxidation charge) compared to Pd crystalline counterpart. Impressive MOR performance and practical scalability of the MG sample dimensions make Pd-Au-Si a potential candidate for micro and macro fuel cell applications.

3.4. MG's in sensor and degradation applications

The advancement in using MG materials in sensor applications is discussed in this section. Phan *et al.* reported MEMS current sensors composed of $Fe_{67.5}B_{22.5}Nd_{6.3}Nb_{3.7}$ magnetic metallic

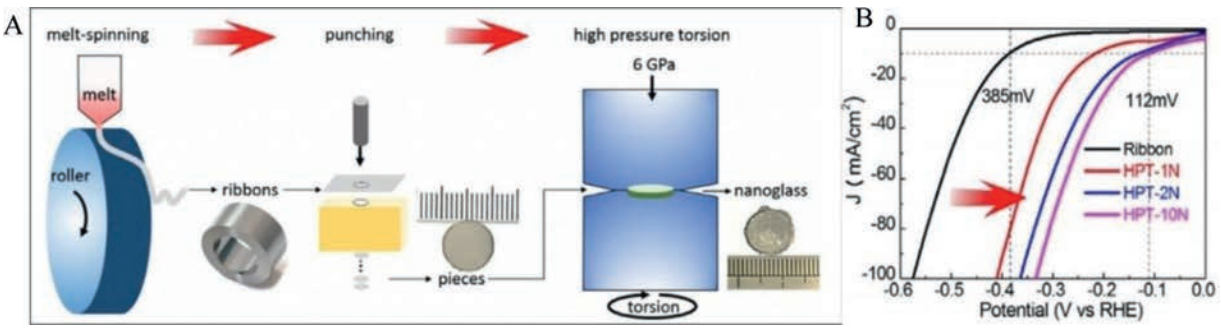

Fig. 7. (A) Schematic illustration for the fabrication of $Fe_{78}Si_9B_{13}$ nanoglass alloy. (B) Linear polarization curves upon HPT treatment. Reproduced with permission [53]. Copyright 2020, Acta Materialia Inc. Published by Elsevier Ltd.

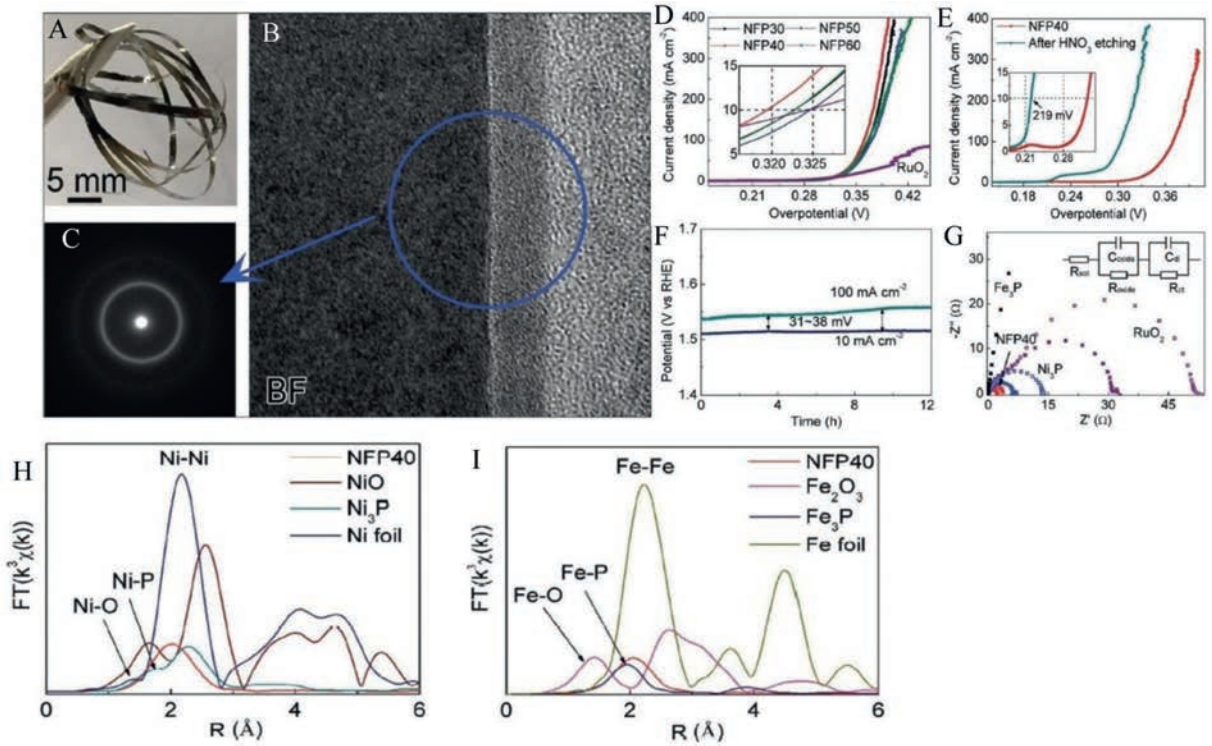

Fig. 8. (A) $Ni_{40}Fe_{40}P_{20}$ MG ribbon for OER catalyst. (B) HRTEM image showing the interface. (C) SAED pattern for the amorphous interface. (D, E) Polarization curves before and after etching. (F) Durability test. (G) EIS spectra for the dealloyed ribbon compared with other catalysts. (H, I) EXAFS spectra. Reproduced with permission [55]. Copyright 2020, Published by WILEY-VCH Verlag GmbH & Co. KGaA, Weinheim.

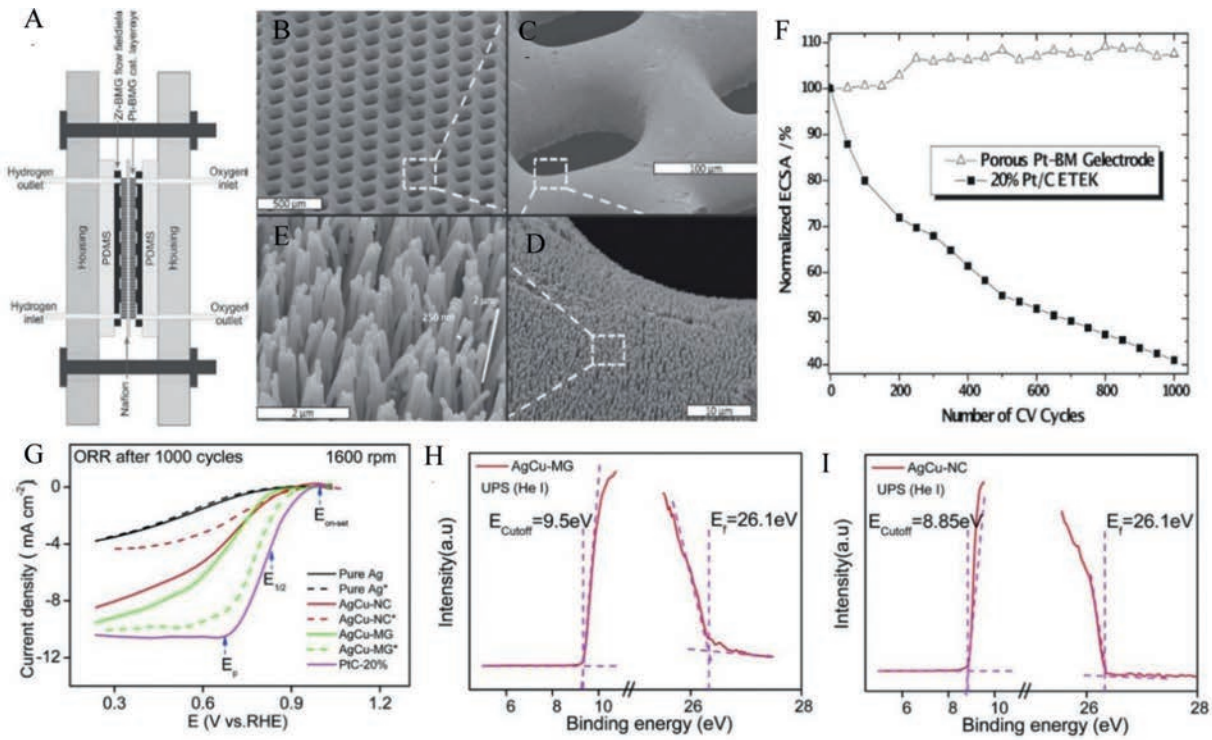

Fig. 9. (A) Micro fuel cell diagram using Zr-BMG flow field/current collector plates and the porous Pt-BMG nanowire catalytic layer architecture. (B-E) SEM images of Pt-BMG nanowire electrode with gas feeding through holes. (F) Loss of the electrochemical surface area (ECSA) after accelerated durability test of porous Pt-BMG electrode and Pt/C (E-TEK) catalysts with the number of cyclic voltammograms (CV) cycles. Reproduced with permission [59]. Copyright 2013, Published by WILEY-VCH Verlag GmbH & Co. KGaA, Weinheim. (G) ORR polarization curve before (shown using solid lines) and after 1000 CV cycle treatments (shown using dashed lines and asterisk (*)) Reproduced with permission [60]. Copyright 2016, the Royal Society of Chemistry. (H, I) Respective E_{cutoff} (energy of the final state) and E_f (energy of the initial state) of AgCu-MG and AgCu-NC measured by UPS. Reproduced with permission [60]. Copyright 2016, the Royal Society of Chemistry.

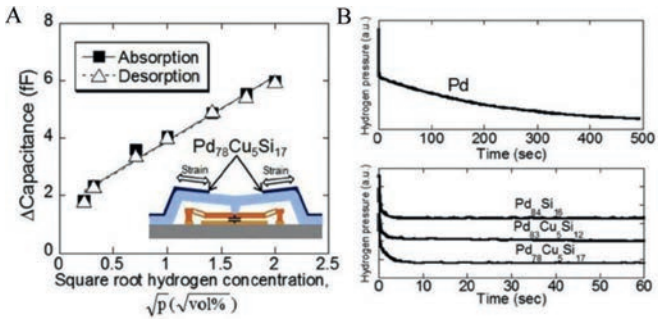

Fig. 10. (A) Capacitance sensitivity of the capacitive MEMS hydrogen sensor with $Pd_{78}Cu_5Si_{17}$ on the membrane (B) Time dependence of pressure during PCT measurement for Pd and Pd-based MG alloys. Reproduced with permission [66]. Copyright 2018, Published by Elsevier Ltd, Hydrogen Energy Publications LLC.

glass thin film (FBNN-MGTF) free-standing cantilever [63]. FBNN-MGTF sensor meets all the requirements for a current sensor to monitor power flow with high reliability, long lifetime, small size, low cost, and ease of installation. FBNN-MGTF is found to be a suitable material for non-contact current sensors based on magnetic field detection with high saturation magnetization (∼0.9 T) and low coercivity (< 20 A/m) with excellent fracture toughness (6.36 MPa $m^{½}$). Minhyuan Jung *et al.* synthesized a multifunctional (pressure/temperature) MG-based electronic skin (e-skin) using $Fe_{33}Zr_{67}$ and $Ni_{50}Ti_{50}$ on a flexible substrate [64]. The MG-based e-skin can detect pressure in the range 100 Pa to 5 kPa and temperature (∼150 °C) with high reliability and low power consumption (∼100 mW), and MGs can be a good choice for the stretchable conductor in soft electronics. N. Nishiyama *et al.* used $Zr_{55}Al_{10}Ni_5Cu_{30}$ glass diaphragm in pressure sensors, and the Zr-MGs exhibited 3.8 times higher sensitivity than conventional SUS630 steel-based diaphragm [65]. Y. Hayashi *et al.* reported $Pd_{78}Cu_5Si_{17}$ MG as a sensing material for capacitive MEMS hydrogen sensors (Fig. 10A) [66]. The response time of PdCuSi MG was two orders of magnitude faster than Pd polycrystals (Fig. 10B).

Metallic glasses exhibit excellent catalytic properties in wastewater treatment by degrading the harmful industrial dye effluents. More reactive sites due to the metastable local structure of MGs have attributed to their superior ability to degrade azo dyes compared to their crystalline counterparts. Iron-based metallic glass has got a lot of attention in catalytic dye degradation. The reductive degradation ability of crystalline zerovalent iron (ZVI) has been successfully applied to degrade organic pollutants [67]. Using ZVI, reactions on the material surface and Fe^0 lose electrons to form ferrous ions (Fe^{2+}): $Fe^0 \rightarrow Fe^{2+} + 2e^-$ and further Fe^{2+} will be oxidized to ferric ion (Fe^{3+}): $Fe^{2+} \rightarrow Fe^{3+} + e^-$ and the electrons generated in the reaction is transferred to organic pollutants for effective degradation. Thus, Fe-based MGs with unique atomic structure and corrosion-resistant than crystalline Fe catalysts attracted vast research interest and have found profound applications as effective catalysts in degrading the harmful organic pollutants with a superior rate. The electrochemical dye degradation of Acid orange II reported by Xindong Qin using $Fe_{78}Si_9B_{13}$ MG ribbon is shown in Fig. 11. Due to the generation of hydroxyl radicals, the electrochemical degradation rate is enhanced and 12 times faster than the chemical degradation rate [68]. Z. Lv *et al*. reported that the ultrasonic (UV) vibration enhanced the inner stored energy of FeSiB MG powder through a structural rejuvenation [69]. The catalytic rejuvenated degradation performance is illustrated in Figs. 12A and B. The microscopic cracks produced on the surface and inside powder during UV vibration provided mass transfer. The author's findings provide a means to reuse the wasted MGs. The energy landscape during structural evolution is given in Fig. 12C. On applying ultrasonic vibration, a rearrangement of the configuration space leads to a substantial minimum of potential energy is seen. Thus the manipulation of wide potential energy range during ultrasonic vibration is possible and thus wide industrial applications, including catalysts. Recently, Chong Yang *et al.* synthesized a three-dimensional hierarchical porous structure $Fe_{68}Mo_5Ni_5Cr_2P_{12.5}C_5B_{2.5}$ MG/copper composite catalysts by 3D printing (Figs. 13A-E) and effectively applied it in wastewater treatments [70]. The authors synthesized MG powder through gas atomization, and the as-printed 3D porous MG/Cu catalysts exhibited high catalytic efficiency in degrading Rhodamine blue dye 620 times higher than the commercial nano zerovalent iron. Figs. 13F-H shows the MG/Cu composite superior degradation rate and COD removal data for RhB and MO dye. The MG/Cu catalysts exhibited 100 times reusability without efficiency loss.

Even though the research on MG based catalysts for degradation applications mainly focuses on the alteration of atomic components, regulation of surface morphology, promotion of electron motion, the effect of introducing crystals in MG matrix, and its impact on catalytic degradation was missing in the literature until Shun-Xing Liang reported a comprehensive study on the impact of crystallization in MGs for practical catalyst applications (Figs. 14A-E) [71]. The authors reported that the as-prepared MG sample ($Fe_{78}Si_9B_{13}$ and $Fe_{73.5}Si_{13.5}B_9Cu_1Nb_3$) exhibited a superior rate of decay following a Fenton-like degradation process. On annealing the sample up to 600 °C, the performance was slightly degraded even though it followed a Fenton-like decay. On further increasing the annealing temperature, the degradation rate improved, as shown in Figs. 14F and G. This rejuvenation in catalyst degradation performance was eventually stabilized to that of the initial performance of as-prepared MG samples. Reasons for the rejuvenated performance are: (1) As the annealing proceeded, structural relaxation occurred, and intermetallic crystalline phases like α-Fe, Fe_2B, and $Fe_{17}Nb_6Si_7$ with electric potential differences facilitated the formation of galvanic cells. (2) During annealing, grain growth caused the shrinking of grain boundaries and promoted more electron transport, and eventually led to rejuvenation in degradation efficiency. Related phenomena have also been observed in other Fe-based MGs. Since all the compositions cannot be achieved in an amorphous metal state, annealing MGs effectively controls grain size, grain boundary, and different potential phases. All these open up exploiting novel electrocatalysts.

4. Modern techniques for developing MG based electrocatalysts

Interdisciplinary researchers working in fabricating MGs and electrochemists together put a lot of effort into the search for the novel use of MGs as potential and robust electrocatalysts for functional applications. It is a proven fact that MG-based electrocatalyst's performance is far superior and industrially favorable than the conventional bulk crystalline catalysts and their nanostructured forms. The enhanced catalytic activity of every electrocatalyst depends on the intrinsic electronic conductivity and the availability of catalytically active sites on the surface while exposed to an electrolyte medium [51,52,72,73]. The current strategy is to generate more active sites or, in other words, increase the electrochemically active surface area (ECSA), development of MGs by selecting suitable elements to improve the electronic conductivity, develop MGs through advanced experimental techniques with more active sites exposed for these electrodes while performing the electrochemical experiment. Some of the evolving modern techniques include high throughput combinatorial screening of MGs with the help of advanced imaging techniques like atom probe tomography (APT) combined with transmission electron microscopy (TEM), theoretical machine language assisted methods, nanostructuring, selective

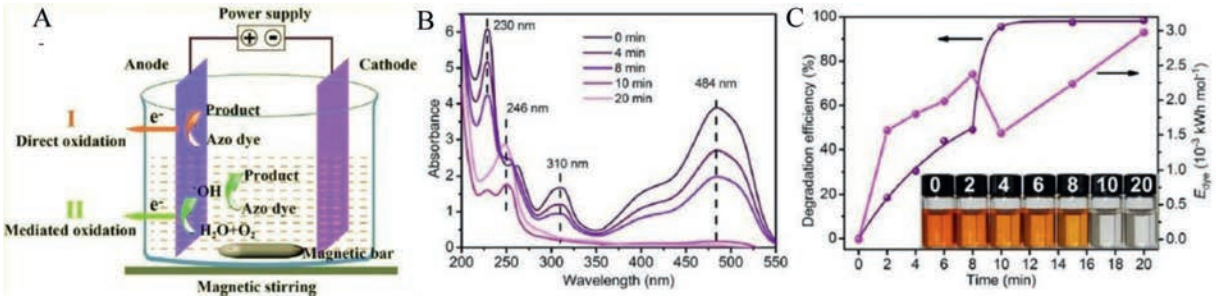

Fig. 11. (A) Schematic illustration of electrochemical degradation of azo dyes using $Fe_{78}Si_9B_{13}$ MG electrodes. (B) UV–vis absorption spectra of AO II aqueous solutions treated with $Fe_{78}Si_9B_{13}$ MG ribbons at a voltage of 1 V for different reaction time, (C) degradation efficiency and specific energy consumption of the electrochemical degradation processes. The inset of (Fig. 11C) is the corresponding photographs of the AO II solution at different reaction times ($C_0 = 0.2$ g/L; E_{dye}: specific energy consumption). Reproduced with permission [68]. Copyright 2018, Published by Elsevier Ltd. on behalf of Journal of Materials Science & Technology.

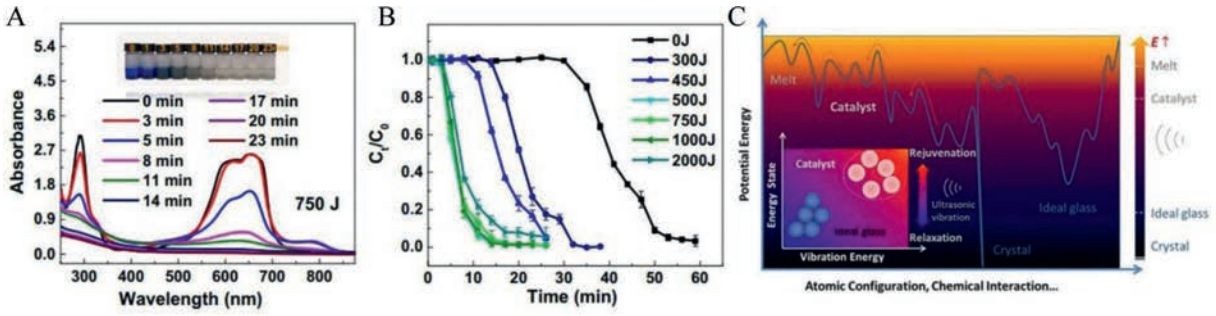

Fig. 12. (A) UV–vis absorbance spectra of MB solutions during the Fenton-like reaction using ultrasonic-vibrated (750 J) $Fe_{78}Si_9B_{13}$ MG powders. (B) The normalized concentration changes of MB solution with different applied ultrasonic energies. (C) Schematic representation of energy landscape in $Fe_{78}Si_9B_{13}$ with the inset showing changes in energy states during structural evolution, including relaxation and rejuvenation. Reproduced with permission [69]. Copyright 2020, Published by Elsevier Ltd. on behalf of Materials & Design.

dealloying. In this section, the recent developments in developing novel MG-based electrocatalysts will be discussed.

4.1. Experimental and computational high throughput screening

Synthesis of a highly functional material focusing on a specific property like catalytic activity depends on tailoring the composition in a wide range. For developing a better performing MG electrocatalyst, tailoring the composition is important while maintaining the intrinsic MG features, including the glass-forming ability (GFA) and metastable features. The intrinsic MG features are sensitive to the atomic percentage of the various elements selected. Several properties of MGs can be tuned by varying the composition. Thus, to promote various applications of MGs, several researchers are attempting to tailor the composition with the available MG fabrication techniques like melt-quenching or mold casting. The conventional synthesis methods are time-consuming for preparing MGs in a wide range of elemental compositions focusing on the specific application like catalysts, sensing, and mechanical applications.

High throughput screening involves fabricating a library of different compositions in a single synthesis step which is evolving as a promising designing approach to materialize MG library consisting of different elemental compositions and discovery of new compositions for a specific application [74–76]. High throughput screening is normally used in drug-related research where hundreds of thousands of experimental samples are simultaneously tested, currently being attempted in optimizing metallic glasses. A combinatorial development of an MG library consisting of thousands of compositions through high throughput screening using physical vapor deposition technique is highly promising for further advancement in this field of research. The composition gradient is formed by varying the sputtering power and tilt angle of the sputtering gun system, as shown in Fig. 15. Jinyang Li reported a Pd–Au–Ag–Ti thin film library (340 measurement areas) and investigated high potential ORR electrocatalysts in the alkaline regime using a scanning droplet cell measurement. The authors found that the lowest overpotential region is shown to be around a quaternary composition region with 30 at% Au and $>$ 7 at% Ag [77].

Through the density functional approach, a computational high throughput screening of MGs for better performing electrocatalysts is attempted [75]. A set of different vital properties such as Gibb's free energy for H_2/O_2 adsorption/desorption in HER and OER, adsorption energy in case of dye degradation catalytic reaction may be determined. By comparing the catalytic parameters of different electrocatalysts in the combinatorial library, a high-performing catalyst may be achieved. The computational approaches in MGs are still in the initial stages of development. Machine learning-assisted high throughput screening for new metallic glasses are reported focusing on structural characteristics. This method essentially deserves attention for designing novel MGs and MGNs based electrocatalysts from large combinatorial MG libraries.

4.2. Nanostructuring of MGs

Nanostructuring metallic glasses to form metallic glass nanostructures (MGNs) with increased active surface area is an important and promising approach to boost electrocatalytic activity. M. Carmo *et al.* reported thermoplastic forming of $Pt_{57.5}Cu_{14.7}Ni_{5.3}P_{22.5}$ BMG to form nanowires and subsequent dealloying to form Pt-BMG nanowires as an efficient HER electrocatalyst shown in Fig. 16 [38].

Bulk metallic glasses, when reheated and formed in the supercooled region (SCLR), the temperature region where glass relaxes into a metastable liquid before it eventually crystallized, a viscosity drop or softening of the BMG in its SCLR occurs. The soften-

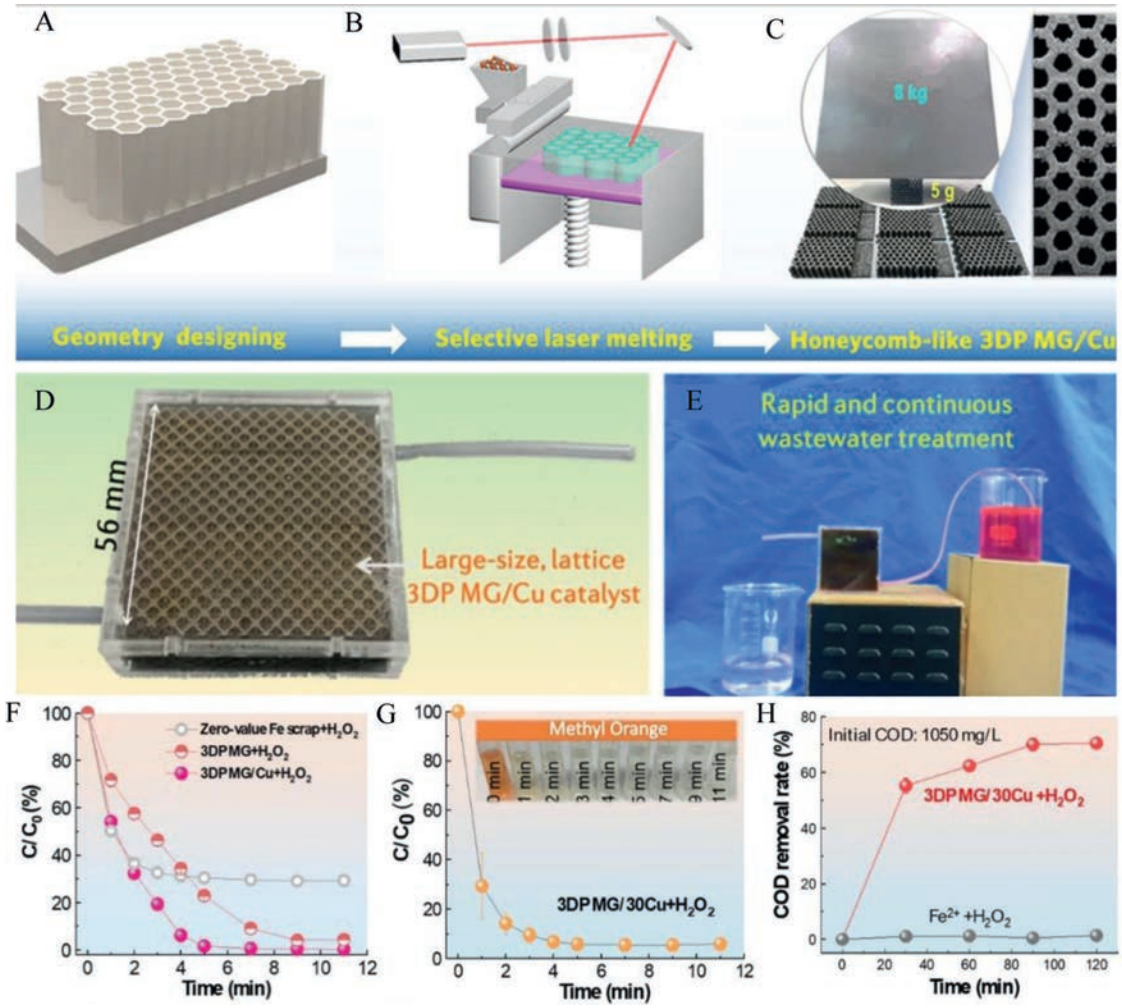

Fig. 13. (A-C) Schematic illustration of the manufacturing processes of MG-based catalysts *via* an SLM 3D printing technique. (A) Compute aided design. (B) Selective laser melting stage. (C) Final Honey comb-like structure of MG/Cu composite. (D) 3D printed Mg/Cu sealed in a polymeric methyl methacrylate (PMMA) cage to construct a flow-through reactor for continuous wastewater treatment. (E) Degradation processes toward the RhB solution. (F) The removal rate of RhB by different catalysts. (G) Removal rate of MO by using the 3DP MG/30Cu as the catalyst. Insets show the rapid decolorization of the solution. (H) COD removal rate toward the dye mixture (RhB + MO) by the MG/Cu catalyst and a Fenton reagent (Fe^{2+}, 20 mg/L). Reproduced with permission [70]. Copyright 2021, Published by American Chemical Society.

ing of BMG at the SCLR can be used for thermoplastic forming to create nano-shaped geometries using template moulding, nanoimprinting even to form hierarchical nanostructures on the surface. The surface area of these nanostructures can even be raised using the dealloying of desired elements at the nanoscale. Thermoplastically formed non-noble metal-based BMGs were reported by Jun Shen *et al.*, which includes Zr-Cu-Al-Y and LaAlNiCuCo BMG [78,79], and the non-noble TPF formed BMGS need to be characterized for electrocatalytic applications. Nanosized MG powder synthesized through gas atomization, ball milling, and further chemical dealloying to form the required composition for various catalyst applications is also being tried, and commendable activity is achieved [80,81]. Schroer's *et al.* introduced a bottom-up method based on multitarget carousel oblique angle deposition (multi-COAD) to fabricate nano-sized MG architectures of tuneable chemistry and controllable three dimensional (3D) shapes with high yield [74]. Wei Yan *et al.* synthesised MG fibres of nanoscale dimensions [82]. The development of electrocatalysts based on these novel methods needs immediate attention.

In order to increase the active surface area or, in other words, to activate the MG electrocatalyst, several techniques were attempted. Nanoporous structure formation through controlled dealloying, surface area enhancements through treatments with ultrasonic vibration (UV), ultrasonic beating forming (UBF), oxygen vacancy creation, dealloying suitable elements to create desirable combinations for optimized catalytic activity were some of the techniques followed and achieved remarkable improvement in catalytic performance [44,69,82–84]. For instance, selecting elements from the two extreme branches of the volcano plot and combining them to form high-performing electrocatalysts for HER is the emerging strategy successfully implemented for the optimization of advanced MG-based electrocatalysts for HER [36]. Nanoporous metals and nonporous structures derived from metallic glass were applied in several catalytic applications. One facile technique is chemical dealloying without using any electric potential or electrochemical dealloying by using an external cell voltage. J.Q. Wang *et al.* reported nanoporous Fe-Si-B-Nb MG for enhanced degradation for azo dye polluted industrial wastewater [85]. The higher efficiency of ball-milled Fe-Si-B-Nb powder is associated with the large surface area of many nanoscale corrugations. The nanoporous electrocatalyst derived from $Ni_{61}Zr_{36}Mo_3$ MG ribbon showed enhanced HER performance toward HER in an alkaline medium (Figs. 17A and B) [45]. The dealloyed NiMo ribbon with a sandwich structure of a nanoporous amorphous layer on the bulk amorphous part. The nanoporous layer consisting of Ov defect sites improved the electronic conductivity, and the

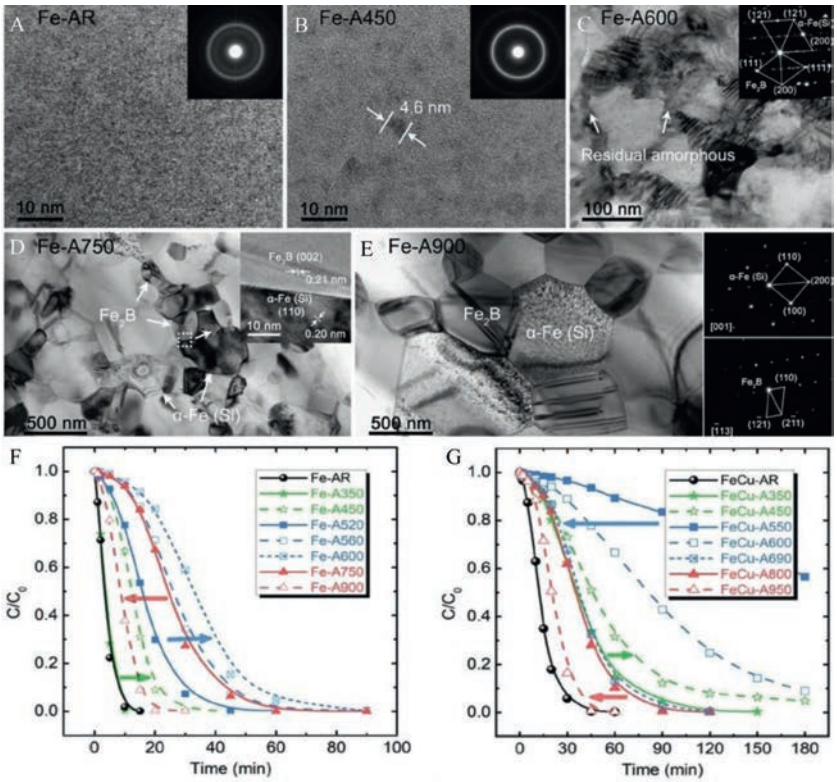

Fig. 14. (A-E) Microstructural evolution of $Fe_{78}Si_9B_{13}$ MG through the as-received state, annealing temperature 450 °C, 600 °C, 750 °C, and 900 °C. (F, G) Effect of annealing temperature on $Fe_{78}Si_9B_{13}$ MG ribbon against the methylene blue catalytic dye degradation rate. Reproduced with permission [71]. Copyright 2018, Published by WILEY-VCH Verlag GmbH & Co. KGaA, Weinheim.

HER activity was efficiently improved than the crystalline counterpart. Yongwen Tan synthesized a hierarchical np-CuMo from Al-CuMO nanocrystalline alloys, and the HER performance was comparable to standard Pt catalysts (Figs. 17C and D) [44]. Molybdenum (Mo) modified hierarchical nanoporous Cu electrocatalyst and nanoporous-CuTiMo, derived by dealloying $Cu_{60}Ti_{37}Mo_3$, showed promising catalytic performance for HER reaction in alkaline medium (Figs. 17E and F) [46]. Nanoporous hierarchical nickel (np-Ni) dealloyed from $Ni_{40}Zr_{40}Ti_{20}$ MG wire using melt spinning technique by moving the remelted ingot towards copper wheel with a wedge angle of 60° at a linear speed of 30 m/s to form circular MG wire of diameter 60 μm showed remarkable HER activity as shown in Figs. 17G and H [39]. The high electrocatalytic activity of $Ni_{40}Zr_{40}Ti_{20}$ MG wire is attributed to the bi-continuous nanoscale ligament-pore structure, which fertilizes active sites. At the same time, good cyclic stability is ascribed to the micrometer-sized slit, which facilitates the release of H_2 gas. Rui Jiang introduced nanoporous-PdFeP catalyst electrochemically dealloyed from $Pd_{10}Fe_{70}P_5C_{15}$ MG ribbon and showed good catalytic activity for HER in acidic medium and is due to bi-continuous nanoporous morphology, amorphous structure, and synergistic effect between non-metallic P and C elements [43]. Jun Shen *et al.* reported the Zr-doped sodium titanate nanobelts prepared by dealloying of Ti-based metallic glassy powders as highly active for the photocat-

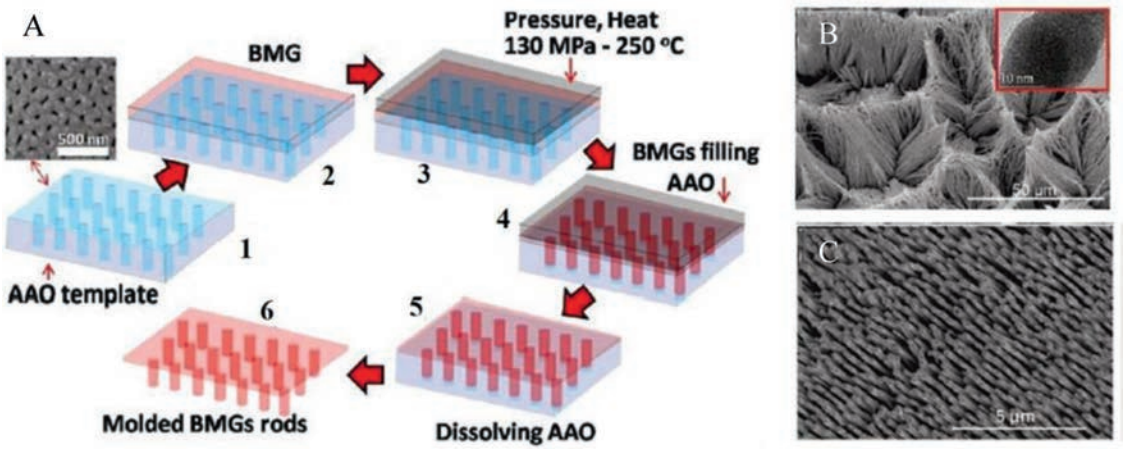

Fig. 16. (A) Schematic TPF forming synthesis of Pt-BMG nanowires in steps 1–6. (B, C) SEM images (TEM image in the inset of B). Reproduced with permission [38]. Copyright 2011, American Chemical Society.

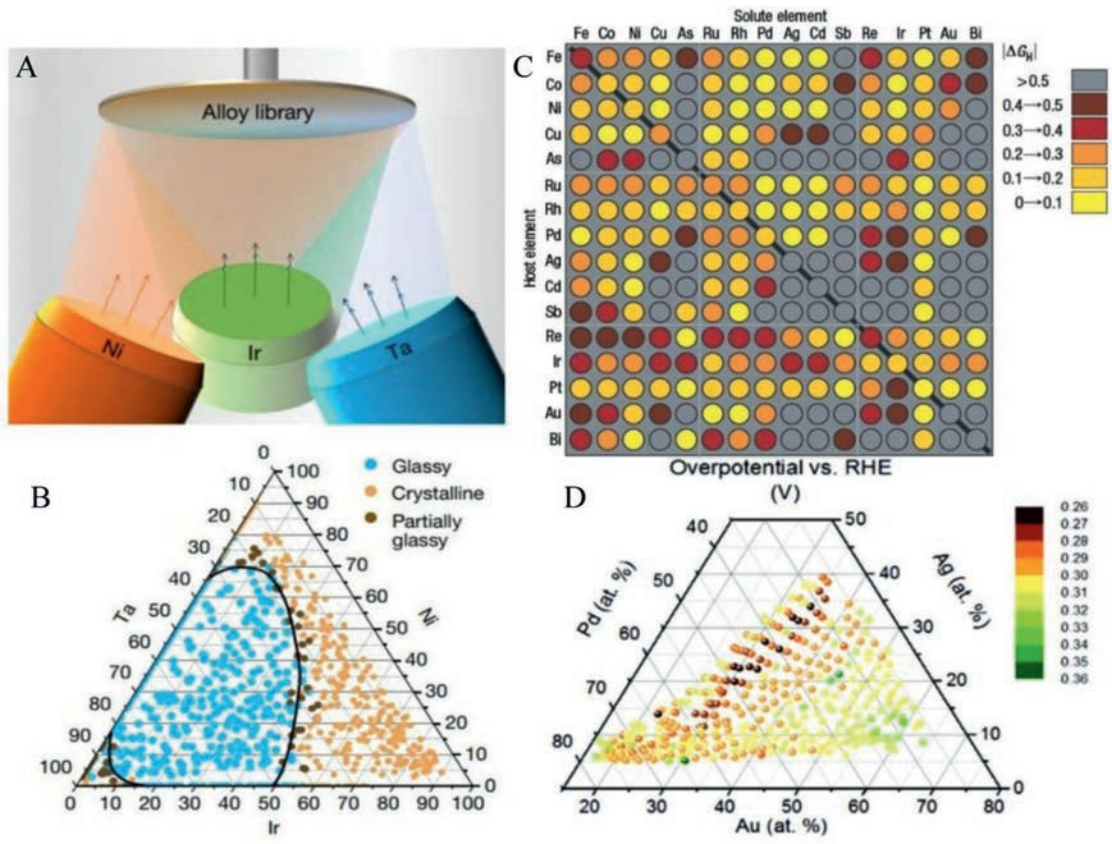

Fig. 15. (A, B) Schematic of magnetron co-sputtering for manufacturing Ir–Ni–Ta BMG system and the glass-forming range of the Ir–Ni–Ta ternary system under high cooling rate by sputtering. Reproduced with permission [75]. Copyright 2019, Nature publishing group. (C) Computational high-throughput screening for HER electrocatalysts based on Gibbs free energy of hydrogen adsorption. The diagonal of the plot corresponds to the hydrogen-adsorption free-energy on the pure metals. Reproduced with permission [76]. Copyright 2006, Nature publishing group. (D) Pd–Au–Ag–Ti thin film library with the composition measured by EDX *vs.* Overpotential for ORR. Reproduced with permission [77]. Copyright 2016, the Royal Society of Chemistry.

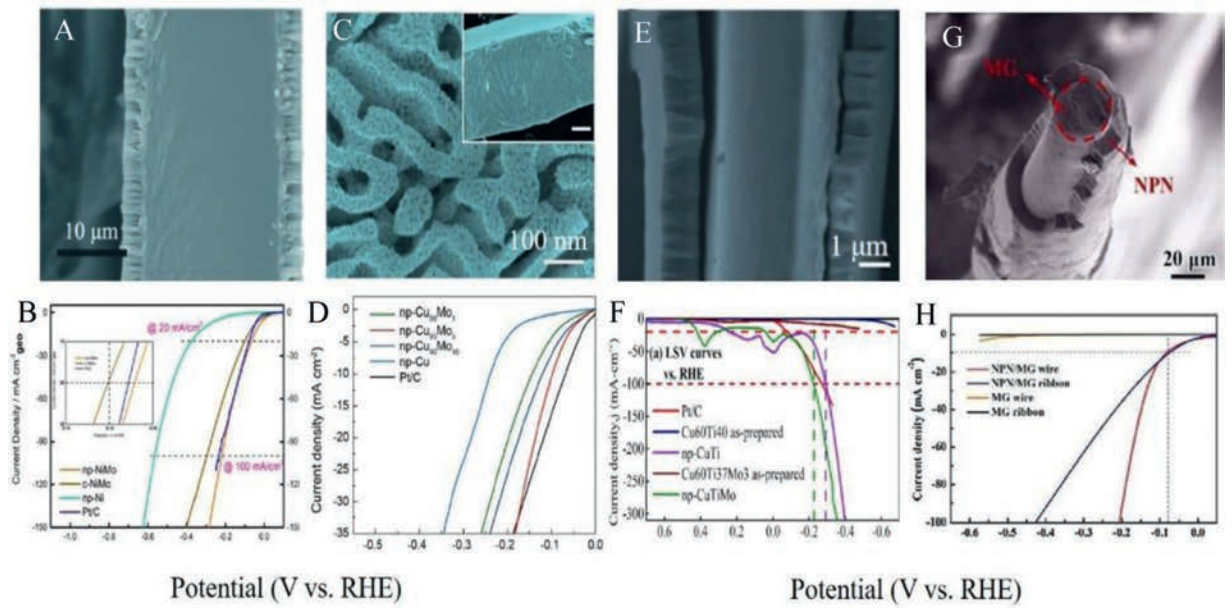

Fig. 17. (A, B) Cross-sectional SEM image and HER polarization curves for dealloyed $Ni_{61}Zr_{36}Mo_3$ MG. Reproduced with permission [45]. Copyright 2020, American Chemical Society. (C, D) Top-view of nanoporous $Cu_{95}Mo_5$ hierarchical structure and HER polarization curves. Reproduced with permission [44]. Copyright 2020, Acta Materialia Inc. Published by Elsevier Ltd. (E, F) Cross-sectional view of dealloyed $Cu_{60}Ti_{37}Mo_3$ and HER polarization curves. Reproduced with permission [46]. Copyright 2021, Elsevier B.V. (G, H) Cross-sectional view of dealloyed $Ni_{40}Zr_{40}Ti_{20}$ MG wire with nanoporous nickel/MG structure and HER polarization curves. Reproduced with permission [39]. Copyright 2021, Published by Elsevier Ltd. on behalf of Journal of Materials Science & Technology.

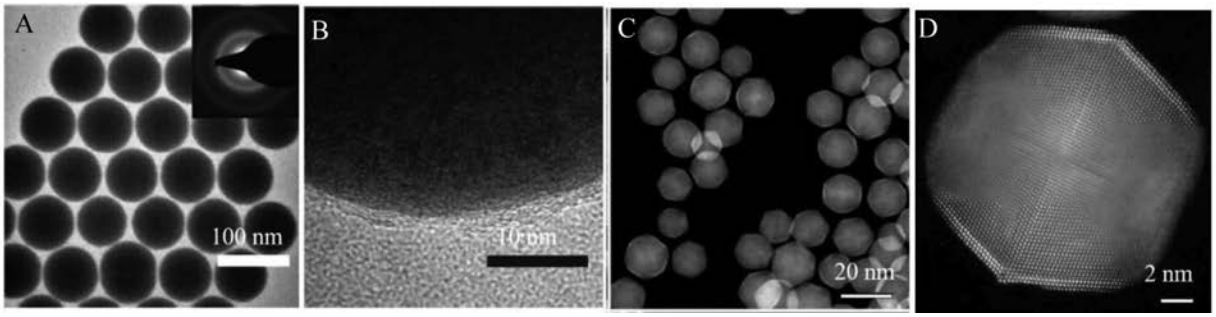

Fig. 18. (A, B) TEM and HRTEM of Ni-B MG nanoparticles synthesized through chemical method (Inset: diffraction pattern). Reproduced with permission [87]. Copyright 2020, Published by American Chemical Society. (C, D) TEM image of Pt@Pd core-shell nanoparticles, atomic resolution HAADF STEM image in Fig. 18D showing layers of Pt in the shell and Pd in the core. Reproduced with permission [91]. Copyright 2015, Nature publishing group.

alytic reaction [86]. It is to be ascertained that dealloying strategy for creating nanoporous/hierarchical versatile structure as an efficient and productive method to enhance the electrocatalytic performance of MGs remarkably equalling to standard precious noble metal-based electrocatalysts.

5. Novel strategies for developing MG-based electrocatalysts

The search for developing novel synthesis techniques for creating advanced metallic glass nanoparticles for catalytic applications is advancing. In this context, the formation of metallic glass nanoparticles *via* colloidal chemical synthesis stands out as a highly promising catalyst for green energy applications (Figs. 18A and B) [87,88]. The important barrier that restricts the wide usage of conventional MGs in different applications is their limited ductility. In crystalline metals or alloys, plastic deformation occurs through the motion of dislocations, which can be modified to an extent and make it more ductile. Meanwhile, deformation of MGs occurs through cooperative shearing of clusters of atoms or shear transformation zones (STZs) [89]. Successive STZs form shear bands and cause sudden catastrophic failure in tension and bending. Metallic glass nanoparticles synthesized *via* colloidal synthesis showed high ductility and an excellent viscoelastic effect upon compression. Even though not found many catalytic applications, the chemically synthesized MG nanoparticles can provide high catalytic activity in terms of enhanced surface area in the nanoscale and improved stability for long-term applications. Sundeep Mukherjee *et al.* introduced a facile pulsed electrodeposition approach to synthesize MG nanowires with even more negligible or nil noble metal content [90]. The MG nanowire through electrodeposition exhibited high electro-oxidation of methanol. Powder metallurgy techniques like gas atomization synthesized MG nanoparticles with improved surface area and core-shell structures fabricated by dealloying techniques are recently getting more attention in catalyst applications. The core and shell of these MG nanoparticles need to be tuned to maximize the surface area and hence improve catalytic activity. Pd-Pt amorphous core-shell nanostructures, as shown in Figs. 18C and D require counterparts in MGs through chemical synthesis and are expected to perform in a much superior manner with less noble metal included [91]. Z. Ding *et al.* reported Core-shell high entropy alloy particles from Fe–Co–Ni–Cr–Nb showed excellent OER properties with an overpotential of 288 mV [92].

6. Reaction mechanism for catalysts

Knowledge of reaction mechanisms and the quantitative/qualitative parameters regarding the active sites available while applying MG materials as catalysts is crucial for designing and implementing high-performing catalysts for energy conversion and storage and for the readers in interdisciplinary research fields. The chemical steps involved in common catalytic reactions like HER are outlined in the discussion, and other reactions follow a similar reaction mechanism not detailed here.

Hydrogen evolution reaction or HER in acidic electrolytes is a significant step in the electrochemical water-splitting reaction. Hydrogen is generated by the electrochemical reduction of protons (H^+) as Eq. 1.

$$2H^+_{aq} + e^- \rightarrow H_2(g) \quad (1)$$

In this reaction, there are two fundamental and widely accepted mechanisms. They are Volmer-Heyrovsky mechanism and Volmer-Tafel mechanisms [93]. Eqs. 1a-c gives the reaction mechanisms in detail along with their corresponding Tafel slopes for HER towards an acidic medium.

$$\text{Volmer step: } H^+ + e^- \rightarrow H_{ads}\text{; Tafel slope: 120 mV/dec} \quad (1a)$$

$$\text{Tafel step: } 2H_{ads} \rightarrow H_2(g)\text{; Tafel slope: 30 mV/dec} \quad (1b)$$

$$\text{Heyrovsky step: } H^+ + H_{ads} + e^- \rightarrow H_2(g)\text{; Tafel slope: 40 mV/dec} \quad (1c)$$

The primary reaction in the case of HER in acidic media is the reduction of two protons (H^+) to give $H_2(g)$. The first step is to make adsorbed hydrogen (H_{ads}) on the catalyst surface by the Volmer reaction, where a proton from the electrolyte solution is reduced at the electrode surface to form H_{ads} with a Tafel slope of 120 mV. The second step is the desorption of the adsorbed hydrogen to hydrogen gas, which proceeds through two alternative routes. One is through Tafel reaction in which two adsorbed hydrogen recombine to form hydrogen gas with a Tafel slope of 30 mV (Eq. 1b). The other alternative route is the Heyrovsky reaction (Eq. 1c), where a hydrated proton binds with H_{ads} through an electron transfer at the electrode surface to form hydrogen gas. This reaction has a Tafel slope of 40 mV. The Tafel slope evaluated from the Tafel plot gives an idea about the intermediate reaction in HER, and this will be the rate-determining reaction.

The rate-determining step of any electrochemical redox reaction is determined using the Tafel slope for the polarization curves or electrochemical impedance from Nyquist curves, and the reaction kinetics can be enhanced by improving the kinetics of this step. But, to design a new metallic glass as a high-performing electrocatalyst, the active sites available for the electrochemical reaction need to be very high. Active site determination and the enhancement in the number of these active sites are crucial in designing high-performing MG catalysts [36,94]. The electrocatalysts for the above-mentioned electrochemical reaction involve the adsorption/desorption of ions of interest (say H^+ ions in HER) from the electrolyte medium. The optimized performance of these catalysts

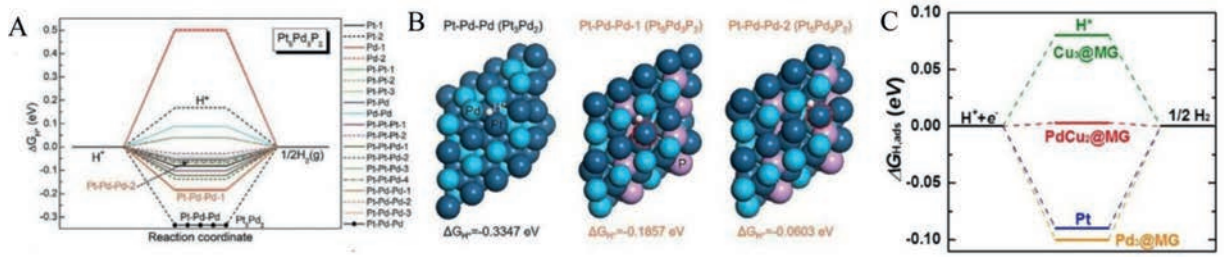

Fig. 19. (A) Gibbs free energy ($\Delta G_H{}^*$) profiles for various top, bridge, and hollow and catalytic sites at the $Pt_5Pd_3P_2$ surface of $Pd_{20}Pt_{20}Cu_{20}Ni_{20}P_{20}$ HEMG. (B) Local chemical environment of H* adsorption on Pt-Pd-Pd hollow sites at Pt_3Pd_2 and $Pt_5Pd_3P_2$. Reproduced with permission [37]. Copyright 2021, Published by WILEY-VCH Verlag GmbH & Co. KGaA, Weinheim. (C) Gibbs free energy ($\Delta G_H{}^*$) profiles for Pd-Ni-Cu-P MG of different active sites with local structures. Reproduced with permission [36]. Copyright 2016, Published by WILEY-VCH Verlag GmbH & Co. KGaA, Weinheim.

occurs when the adsorption and desorption proceed not too fast, not too slow manner. In other words, if the rate of either adsorption or desorption is low, the overall reaction gets affected, and the overall rate of reaction reduces. The rate of reaction can be maintained at a high pace by maintaining a thermoneutral ($\Delta G_f \sim 0$) free energy value. Thus, the elements for synthesizing an MG-based electrocatalyst for HER may be selected so that the free energy for hydrogen adsorption/desorption ($\Delta G_H \sim 0$) is nearly close to zero [95]. The Gibb's free energy is dependent directly on the electronic structure of the catalyst. Thus, through the theoretical approach, the species with thermoneutral free energy are identified as active sites for the HER. Using DFT calculations, a more significant number of active sites may be identified, and the quantification of the maximum number of active sites leads to the discovery of high-performing electrocatalysts. It should be ascertained that DFT-assisted indirect determination needs to be combined with advanced imaging characterizations for better engineering of the active sites and better catalytic activity.

High entropy metallic glasses (HEMGs) with at least five elements with equal atomic fractions range from 5 at% to 35 at% were studied for electrocatalytic applications recently. The synergistic effect of multiple combinations of different elements in HEMG can contribute towards high catalytic activity. Using DFT calculations, the local active sites available for catalytic activity were determined. $Pd_{20}Pt_{20}Cu_{20}Ni_{20}P_{20}$ HEMG was observed to be a highly active electrocatalyst for HER, with their nanosponge architecture developed through dealloying treatment (Figs. 19A and B) [37]. The Pt_3Pd_2 site showed a lower ΔG_H value (–0.3347 eV) which promoted the adsorption Volmer reaction, while $Pt_5Pd_3P_2$ with adsorption energy –0.02 eV promoted Heyrovsky reaction. With the Volmer and Heyrovsky reaction involved at a high rate, these two types of active sites contribute to the overall increase in HER kinetics. From DFT calculations, Hu *et al.* revealed $PdCu_2$ active site in PdNiCuP has thermoneutral energy ($\Delta G_H \sim 0$ eV) and is shown in the free energy diagram for hydrogen adsorption in PdNiCuP MG in Fig. 19C [36].

Exploring the active sites in 2D materials like graphene-based catalysts, layered MoS_2, and their modifications to increase the number of available active sites is worked out by several electrochemists. By introducing edge and defect sites, *i.e.*, inducing armchair and zigzag edges, the electronic density of states present in graphene is enhanced. Using DFT calculation, Deng *et al.* found that ORR can proceed along the zigzag edges of graphene with ball milling is employed to enhance the ORR activity by increasing the zigzag edge density as shown in Fig. 20 [96,97]. Therefore, the determination of active sites in metallic glass-based catalysts and the engineering of these active sites to promote catalytic activity requires immediate attention. It may be observed that the synergistic effect of constituent elements in MGs and the presence of local metastable structures are unique features for high catalytic performance. In contrast, in crystalline catalysts, the structure itself plays

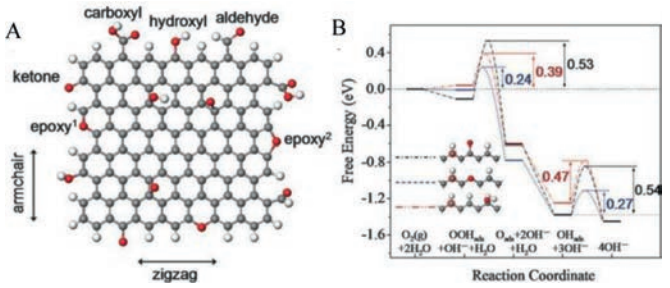

Fig. 20. (A) Schematic diagram of nanographene showing armchair and zigzag edges with oxygen-containing groups (C-gray, O-red, H-white). (B) The free energies for elementary steps along the reaction coordinate in ORR on the zigzag edge of graphene. Sites for dotted line with the active sites marked in red circles. Reproduced with permission [96]. Copyright 2011, Published by the Royal Society of Chemistry.

a role in catalytic performance. The enhancement of the active catalytic sites in MGs and MGNs by proper engineerings like correlative microscopy technique using three-dimensional atom probe tomography (3D-APT) and TEM for grain boundary segregation engineering (GBSE) is a unique novel approach [98,99]. Grain boundary segregation leads to nanoscale chemical variation, which alters material performance by orders of magnitude, and GBSE using correlative APT (Figs. 21A and B) is the only existing technique available for near-atomic scale characterization and needs immediate attention for discovering high performing MG based catalysts [100]. Pradeep *et al.* reported the rapid annealing induced primary crystallization of Fe-Si nanocrystals in $Fe_{73.5}Si_{15.5}Cu_1Nb_3B_7$ MG alloy using APT [99]. The APT map of Cu clusters at different annealing temperatures in Figs. 21C-H. The APT results illustrated that the Cu clusters initially induced a local enrichment of Fe and Si in the amorphous matrix. The local chemical heterogeneities are seen to be the actual nuclei for subsequent nano crystallization. The structural correlation length is much smaller than the domain wall width leading to small magneto crystalline anisotropy or coercivity and the MG nanocrystals were found to be applicable as low loss small coercive soft magnets. Thus, applying APT, MG alloys can be studied in the atomic level and novel applications for MG including high performing catalyst may be achieved.

Even some of the MGs showed a self-stabilized behavior, leading to an enhancement in catalytic activity upon cycling for a longer time [36,52]. This case is different from the crystalline catalyst in which the activity deteriorates with the reduced number of active sites on continuous cycling. The self-stabilized improved catalytic activity for MGs on cycling is due to the self-optimization of the active sites from a self-dealloying process during the reaction. Thus, a focused study on the atomic scale features of the active sites through 3D-APT correlative microscopy and *in-situ* measurements like electrochemical scanning microscopy, *in-situ* spectroelectrochemical measurements needs to be considered.

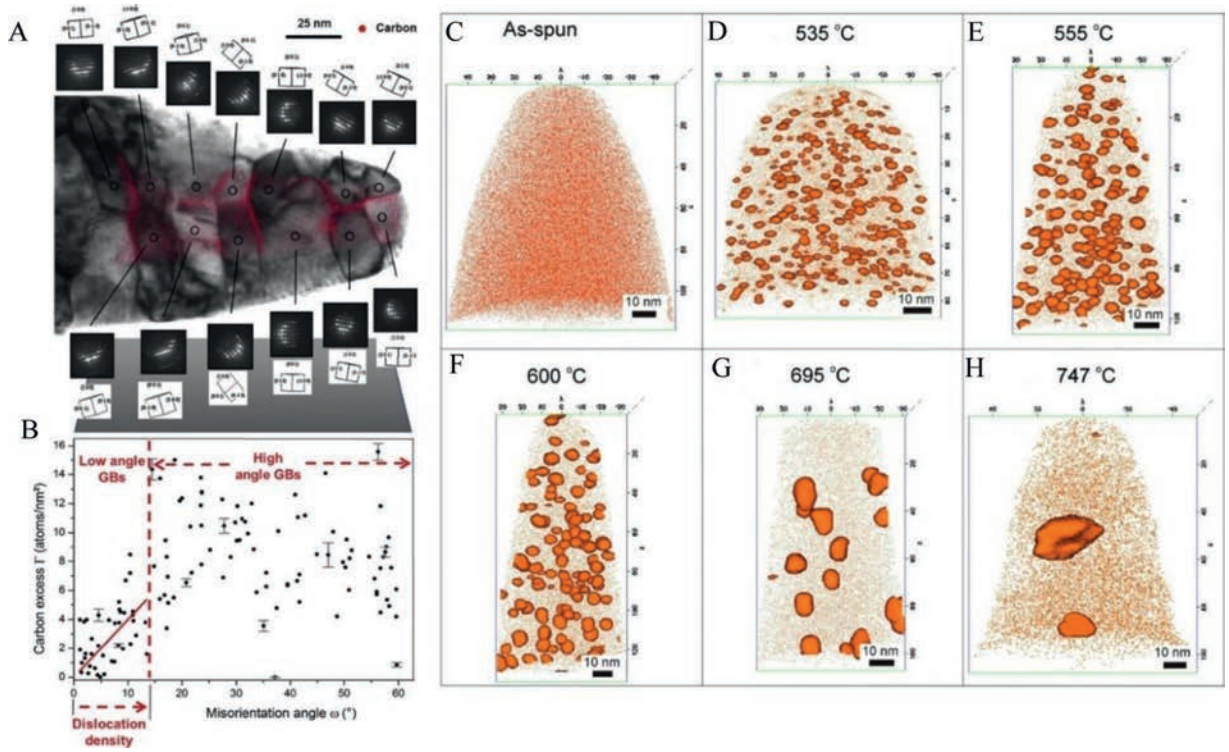

Fig. 21. (A, B) Correlative 3D-APT image and TEM with 3D atom map provided by nanobeam electron diffraction, applied for carbon GB segregation in ferrite. Investigating nanocrystalline materials containing multiple GBs per APT sample allows for high throughput while maintaining excellent spatial and chemical resolution. The segregation data in Fig. 21B was obtained from 121 GBs on seven different APT tips measured in six days of experimental time. Reproduced with permission [90]. Copyright 2014, Elsevier Ltd on behalf of Current Opinion in Solid State and Materials Science. (C-H) APT elemental maps of Cu and Cu-rich clusters delineated by 3 at% isoconcentration surfaces when the as-prepared amorphous alloy is rapidly annealed for 4 s over a range of annealing temperatures: (C) as-prepared amorphous, (D) 535 °C, (E) 555 °C, (F) 600 °C, (G) 695 °C, (H) 747 °C. Reproduced with permission [100]. Copyright 2014, Published by the Royal Society of Chemistry. Elsevier Ltd. on behalf of Acta Materialia.

7. Concluding remarks, outlook and opportunities

Metallic glasses or amorphous metals are long-range disordered at the macroscopic level but short-range ordered at the nanoscale level. In this brief review, we summarized metallic glasses and their nanostructured forms used for catalyzing various electrochemical reactions, and some novel applications were highlighted. At the short-range order, metallic glasses have *quasi* nanocluster-like structures and are randomly packed with micro defects. At the long-range order, the metallic glasses have a uniform topological order. Defect-free structured single-phase MGs with high entropy are highly advantageous for catalytic applications in addition to structural applications. Recently the functional applications of MGs showed a boom among the researchers working in interdisciplinary applications of metallic glasses like catalytic studies. The rejuvenated interest arises due to the nanostructures grown on the surface of MGs and the fully crystalline phases evolved from metastable MG structures. The advantage of metallic glass nanostructures is that the limited GFA of MG forming a combination of elements can be ignored. The functional applications of MGs and MGNs need to be promoted for large-scale industrial applications. According to scientists, the key indicators for MGs in various functional applications are high material strength, elastic, and corrosion-resistant. For catalytic applications, large surface area, effective mass and ion transport, presence of surface charges arising long-range disorder and high entropy is required. The recent development of high entropy metallic glasses is of high potential for these applications. It was observed that the catalytic efficiency of MG-based electrocatalysts mainly depends on the composition of various elements and the availability of active surface sites. Recent developments like metallic glass nanostructuring and novel strategies to optimize the catalytic performance comparable to standard noble metal-based catalysts are also discussed. The availability of an increased number of active sites and excellent durability of MG-based catalysts is considered as the new route for the future design of highly efficient catalysts in the field of green energy conversion. Even though MGs and their nanostructured forms have the above-said merits for catalytic applications, there are as many hurdles/challenges to be overcome for the researchers as well as industrialists. The main challenges for developing MG based catalysts are listed below:

- The main issue is that not all the compositions are difficult to realize in metallic glassy form. The glass-forming ability and availability of a wide supercooled temperature range are some of the barriers to overcome for the successful development of metallic glasses showing excellent efficiency for catalyst applications.
- Even though noble metals show high intrinsic electrocatalytic activity, the strong metallic bonds present in noble metals hinder the development of noble metal-based MG electrocatalysts. Noble metal-based MG electrocatalysts have superior catalytic activity than non-noble metal-based MG catalysts. Attempts to improve the non-noble metal MGs are still in progress.
- Quantitative characterization of short-range order is still not achieved. The exact amount of amorphous phase and crystalline phase in metallic glass is an important parameter for developing high-performing industrial electrocatalysts.
- The improvement of corrosion stability of transition metal-based electrocatalysts needs to be considered. Theoretical study of the complex disordered MG structures correlating with corrosion-related parameters needs to be reported for developing MG-based electrocatalysts with high efficiency.

- Industrial production of literature reported highly efficient MG-based catalysts is of importance. Currently, FeSiB MG is the bulk manufactured alloy on an industrial scale. Other compositions need to be manufactured in bulk for various applications.

For the future direction, some of the strategies may be pointed as follows:

- Designing metallic glass-based catalysts using novel nano architectures and development of high entropy metallic glasses.
- Improve the surface area of the MG-based electrocatalysts using selective dealloying on dual-phased amorphous nanocrystalline metallic glass composites.
- Preparation of low dimensional materials like 2D materials using metallic glasses embedded in carbon material hosts like carbon nanotubes, 2-dimensional graphene, layered structures like MoS_2, WS_2, *etc.*
- Exploring spherical-shaped metallic glass nanoparticles through novel chemical synthesis techniques.
- Use of high throughput screening combined with machine learning approach for implementing MG libraries for optimized catalytic performance.

In-situ measurements of advanced characterizations like *in-situ* X-ray absorption spectroscopy, *in-situ* TEM, combined with DFT techniques, can give detailed information regarding the active sites while performing the catalytic reaction. Grain boundary segregation engineering using 3D-APT and TEM is the advanced characterization proposed to design MG-based novel electrocatalysts. This approach can be used to design advanced catalysts with more catalytic active sites and enhanced efficiency.

Thus, the perspectives mentioned above will be insightful for developing novel catalysts for various functional applications.

Declaration of competing interest

The authors declare no conflict of interest.

Acknowledgment

This work is supported by the China National Natural Science Foundation (No. 52071217).

References

[1] W. Klement, R.H. Willens, P.O.L. Duwez, Nature 187 (1960) 869–870.
[2] A.L. Greer, Science 267 (1995) 1947–1953.
[3] M.Z. Ma, R.P. Liu, Y. Xiao, et al., Mater. Sci. Eng. A 386 (2004) 326–330.
[4] M.F. Ashby, A.L. Greer, Scr. Mater. 54 (2006) 321–326.
[5] H.F. Li, Y.F. Zheng, Acta Biomater 36 (2016) 1–20.
[6] Y.C. Hu, C. Sun, C. Sun, ChemCatChem 11 (2019) 2401–2414.
[7] L.C. Zhang, S.X. Liang, Chem. Asian J. 13 (2018) 3575–3592.
[8] Y.Q. Cheng, E. Ma, H.W. Sheng, Phys. Rev. Lett. 102 (2009) 245501.
[9] H.W. Sheng, W.K. Luo, F.M. Alamgir, J.M. Bai, E. Ma, Nature 439 (2006) 419–425.
[10] Y. Yang, J. Zhou, F. Zhu, et al., Nature 592 (2021) 60–64.
[11] A. Hirata, P. Guan, T. Fujita, et al., Nat. Mater. 10 (2011) 28–33.
[12] A. Hiratal. J. Kang, T. Fujita, et al., Science 341 (2013) 376–379.
[13] Y. Hirotsu, T.G. Nieh, A. Hirata, T. Ohkubo, N Tanaka, Phys. Rev. B 73 (2006) 012205.
[14] L. Tian, Y.Q. Cheng, Z.W. Shan, et al., Nat. Commun. 3 (2012) 609.
[15] T. Zhang, Q. Yang, Y. Ji, et al., Chin. Sci. Bull. 56 (2011) 3972–3977.
[16] Z. Jia, X. Duan, W. Zhang, et al., Sci. Rep. 6 (2016) 38520.
[17] G. Kumar, H.X. Tang, J. Schroers, Nature 457 (2009) 868–872.
[18] L. Liu, M. Hasan, G. Kumar, Nanoscale 6 (2014) 2027–2036.
[19] H.B. Yu, Y. Luo, K. Samwer, Adv. Mater. 25 (2013) 5904–5908.
[20] Z.J. Wang, M.X. Li, J.H. Yu, et al., Adv. Mater. 32 (2020) 1906384.
[21] S. Pauly, L. Löber, R. Petters, et al., Mater. Today 16 (2013) 37–41.
[22] C. Yang, C. Zhang, W. Xing, L. Liu, Intermetallics 94 (2018) 22–28.
[23] B.H.R. Suryanto, Y. Wang, R.K. Hocking, W. Adamson, C. Zhao, Nat. Commun. 10 (2019) 5599.
[24] C. Sun, J.A. Alonso, J. Bian, Adv. Energy Mater. 11 (2021) 2000459.
[25] Y. Li, H. Wang, L. Xie, et al., J. Am. Chem. Soc. 133 (2011) 7296–7299.
[26] S. Yuan, S.Y. Pang, J. Hao, Appl. Phys. Rev. 7 (2020) 21304.
[27] I.K. Mishra, H. Zhou, J. Sun, et al., Mater. Today Phys. 4 (2018) 1–6.
[28] J.S. Kang, J. Kim, M.J. Lee, et al., Adv. Sci. 5 (2018) 1700601.
[29] T. Guo, Y. Song, Z. Sun, et al., J. Energy Chem. 42 (2020) 34–42.
[30] G. Giuffredi, A. Mezzetti, A. Perego, et al., Small 16 (2020) 2004047.
[31] J. Zhang, C. Zhang, Z. Wang, et al., Small 14 (2018) 1703098.
[32] D.H. Kweon, M.S. Okyay, S.J. Kim, et al., Nat. Commun. 11 (2020) 1278.
[33] J. Yu, T. Zhang, Y. Sun, et al., SmallACS Appl. Mater. Interfaces 12 (2020) 12783–12792.
[34] Y. Zheng, Y. Jiao, Y. Zhu, et al., Nat. Commun. 5 (2014) 3783.
[35] A. Li, Y. Sun, T. Yao, H. Han, Chem. Eur. J. 24 (2018) 18334–18355.
[36] Y.C. Hu, Y.Z. Wang, R. Su, et al., Adv. Mater. 28 (2016) 10293–10297.
[37] Z. Jia, K. Nomoto, Q. Wang, et al., Adv. Funct. Mater. 31 (2021) 2101586.
[38] M. Carmo, R.C. Sekol, S. Ding, et al., ACS Nano 5 (2011) 2979–2983.
[39] J. Wang, L. You, Z. Li, et al., J. Mater. Sci. Technol. 73 (2021) 145–150.
[40] M. Zhao, K. Abe, S. Yamaura, Y. Yamamoto, N. Asao, Chem. Mater. 26 (2014) 1056–1061.
[41] X. Yang, W. Xu, S. Cao, et al., Appl. Catal. B: Environ. 246 (2019) 156–165.
[42] R. Li, X. Liu, R. Wu, et al., Adv. Mater. 31 (2019) 1904989.
[43] R. Jiang, Z. Cui, W. Xu, et al., Electrochim. Acta 328 (2019) 135082.
[44] M. Luo, W. Peng, Y. Zhao, et al., Scr. Mater. 191 (2021) 56–61.
[45] Y. Zhu, Y. Pan, W. Dai, T. Lu, ACS Appl. Energy Mater. 3 (2020) 1319–1327.
[46] K.S. Aneeshkumar, J. Tian, J. Shen, J. Alloys Compd. 886 (2021) 161270.
[47] K.S. Aneeshkumar, J. Tseng, X. Liu, et al., RSC Adv. 11 (2021) 7369–7380.
[48] H.W. Liang, S. Brüller, R. Dong, et al., Nat. Commun. 6 (2015) 7992.
[49] Y. Yan, C. Wang, Z. Huang, et al., J. Mater. Chem. A 9 (2021) 5415–5424.
[50] F. Chu, B. Han, K. Edalati, et al., Scr. Mater. 204 (2021) 114145.
[51] F. Zhang, J. Wu, W. Jiang, Q. Hu, B. Zhang, ACS Appl. Mater. Interfaces 9 (2017) 31340–31344.
[52] Y. Tan, F. Zhu, H. Wang, et al., Adv. Mater. Interfaces 4 (2017) 1601086.
[53] K. Wu, Y. Meng, J. Xu, et al., Scr. Mater. 188 (2020) 135–139.
[54] C.C.L. McCrory, S. Jung, I.M. Ferrer, et al., J. Am. Chem. Soc. 137 (2015) 4347–4357.
[55] S. Jiang, L. Zhu, Z. Yang, Y. Wang, Electrochim. Acta 368 (2021) 137618.
[56] F. Hu, S. Zhu, S. Chen, et al., Adv. Mater. 29 (2017) 1606570.
[57] A. Pozio, F. Zaza, A. Masci, R.F. Silva, J. Power Sources 179 (2008) 631–639.
[58] X. Han, S. Feng, S. Chen, et al., Int. J. Hydrogen Energy 45 (2020) 3132–3144.
[59] R.C. Sekol, G. Kumar, M. Carmo, et al., Small 9 (2013) 2081–2085.
[60] X. Wu, F. Chen, N. Zhang, et al., J. Mater. Chem: A 4 (2016) 3527–3537.
[61] R.C. Sekol, M. Carmo, G. Kumar, et al., Int. J. Hydrogen Energy 38 (2013) 11248–11255.
[62] B. Sarac, T. Karazehir, Y.P. Ivanov, et al., Nanoscale 12 (2020) 22586–22595.
[63] T.A. Phan, M. Hara, H. Oguchi, et al., Microelectron. Eng. 135 (2015) 28–31.
[64] M. Jung, E. Lee, D. Kim, et al., Npj Flex. Electron. 3 (2019) 8.
[65] N. Nishiyama, K. Amiya, A. Inoue, J. Non. Cryst. Solids 353 (2007) 3615–3621.
[66] Y. Hayashi, H. Yamazaki, D. Ono, et al., Int. J. Hydrogen Energy 43 (2018) 9438–9445.
[67] J. Yan, L. Qian, W. Gao, et al., Sci. Rep. 7 (2017) 43051.
[68] X. Qin, Z. Li, Z. Zhu, et al., J. Mater. Sci. Technol. 34 (2018) 2290–2296.
[69] Z. Lv, Y. Yan, C. Yuan, et al., Mater. Des. 194 (2020) 108876.
[70] C. Yang, C. Zhang, Z.J. Chen, et al., ACS Appl. Mater. Interfaces 13 (2021) 7227–7237.
[71] S.X. Liang, Z. Jia, Y.J. Liu, et al., Adv. Mater. 30 (2018) 1802764.
[72] S. Xie, P. Huang, J.J. Kruzic, et al., Sci. Rep. 6 (2016) 21947.
[73] V. Hasannaeimi, S. Mukherjee, Sci. Rep. 9 (2019) 12136.
[74] S. Ding, Y. Liu, Y. Li, et al., Nat. Mater. 13 (2014) 494–500.
[75] J. Greeley, T.F. Jaramillo, J. Bonde, et al., Nat. Mater. 5 (2006) 909–913.
[76] M.X. Li, S.F. Zhao, Z. Lu, et al., Nature 569 (2019) 99–103.
[77] J. Li, H.S. Stein, K. Sliozberg, et al., J. Mater. Chem. A 5 (2017) 67–72.
[78] S. Cheng, J. Zhu, J. Shen, X. Wei, J. Alloys Compd. 872 (2021) 159684.
[79] J. Fu, Z. Huang, J. Yang, J. Ma, J. Shen, J. Non. Cryst. Solids 558 (2021) 120682.
[80] D.J. Wang, Z.H. Li, M.A. Rahman, J. Shen, Langmuir 29 (2013) 8108–8115.
[81] D. Wang, Y. An, S. Gao, Appl. Surf. Sci. 506 (2020) 144871.
[82] W. Yan, I. Richard, G. Kurtuldu, et al., Nat. Nanotechnol. 15 (2020) 875–882.
[83] M. Meng, R. Li, L. Zuo, et al., Scr. Mater. 199 (2021) 113884.
[84] M. Fang, W. Gao, G. Dong, et al., Nano Energy 27 (2016) 247–254.
[85] J.Q. Wang, Y.H. Liu, M.W. Chen, et al., Adv. Funct. Mater. 22 (2012) 2567–2570.
[86] D.J. Wang, Z.H. Li, Y.L. An, et al., Int. J. Hydrogen Energy 37 (2012) 8240–8248.
[87] M.T. Kiani, C.M. Barr, S. Xu, et al., Nano Lett. 20 (2020) 6481–6487.
[88] M.T. Kiani, K. Hattar, X.W. Gu, ACS Appl. Mater. Interfaces 12 (2020) 40910–40916.
[89] A.S. Argon, Acta Metall 27 (1979) 47–58.
[90] V. Hasannaeimi, X. Wang, R. Salloom, et al., ACS Appl. Energy Mater. 3 (2020) 12099–12107.
[91] X. Wang, S.I. Choi, L.T. Roling, et al., Nat. Commun. 6 (2015) 7594.
[92] Z. Ding, J. Bian, S. Shuang, et al., Adv. Sustain. Syst. 4 (2020) 1900105.
[93] N. Dubouis, A. Grimaud, Chem. Sci. 10 (2019) 9165–9181.
[94] J. Huang, Y. Jiang, T. An, M. Cao, J. Mater. Chem. A 8 (2020) 25465–25498.
[95] S. Sarkar, S.C. Peter, Inorg. Chem. Front. 5 (2018) 2060–2080.
[96] D. Deng, L. Yu, X. Pan, et al., Chem. Commun. 47 (2011) 10016–10018.
[97] D. Deng, K.S. Novoselov, Q. Fu, et al., Nat. Nanotechnol. 11 (2016) 218–230.
[98] D. Raabe, M. Herbig, S. Sandlöbes, et al., Curr. Opin. Solid State Mater. Sci. 18 (2014) 253–261.
[99] K.G. Pradeep, G. Herzer, P. Choi, D. Raabe, Acta Mater. 68 (2014) 295–309.
[100] M. Herbig, D. Raabe, Y.J. Li, et al., Phys. Rev. Lett. 112 (2014) 126103.